

# Increased Drag Coefficient in Estuarine Channels with Curvature

Tong Bo<sup>1</sup> and David Keith Ralston<sup>2</sup>

<sup>1</sup>MIT, WHOI

<sup>2</sup>Woods Hole Oceanographic Institution

November 21, 2022

## Abstract

Flow separation has been observed and studied in sinuous laboratory channels and natural meanders, but the effects of flow separation on along-channel drag are not well understood. Motivated by observations of large drag coefficients from a shallow, sinuous estuary, we found in idealized numerical models representative of that system that flow separation in tidal channels with curvature can create form drag that increases the total drag to more than twice that from bottom friction alone. In the momentum budget, the pressure gradient is balanced by the combined effects of bottom friction and form drag, which is calculated directly. The effective increase in total drag coefficient depends on two geometric parameters: dimensionless water depth and bend sharpness, or the bend radius of curvature to channel width ratio. We introduce a theoretical boundary layer separation model to explain this parameter dependence and to predict flow separation and the increased drag. The drag coefficient can increase by a factor of 2 - 7 in “sharp” and “deep” sinuous channels where flow separation is most likely. Flow separation also enhances energy dissipation due to increased velocities, resulting in greater loss of tidal energy and weakened stratification. Flow separation and the associated drag increase are expected to be more common in meanders of tidal channels than rivers, where point bars that inhibit flow separation are more commonly found. The increased drag due to flow separation affects the tidal amplitude and phasing along the estuary and creates potential morphological feedbacks.

# Increased Drag Coefficient in Estuarine Channels with Curvature

Tong Bo<sup>1,2,\*</sup> and David K. Ralston<sup>2</sup>

<sup>1</sup>MIT-WHOI Joint Program, Cambridge, MA 02139, United States

<sup>2</sup>Woods Hole Oceanographic Institution, Applied Ocean Physics and Engineering, Woods Hole, MA 02543, United States

\*Corresponding author: Tong Bo, tongbo@mit.edu

March 20, 2020

## Abstract

Flow separation has been observed and studied in sinuous laboratory channels and natural meanders, but the effects of flow separation on along-channel drag are not well understood. Motivated by observations of large drag coefficients from a shallow, sinuous estuary, we found in idealized numerical models representative of that system that flow separation in tidal channels with curvature can create form drag that increases the total drag to more than twice that from bottom friction alone. In the momentum budget, the pressure gradient is balanced by the combined effects of bottom friction and form drag, which is calculated directly. The effective increase in total drag coefficient depends on two geometric parameters: dimensionless water depth and bend sharpness, or the bend radius of curvature to channel width ratio. We introduce a theoretical boundary layer separation model to explain this parameter dependence and to predict flow separation and the increased drag. The drag coefficient can increase by a factor of 2 – 7 in “sharp” and “deep” sinuous channels where flow separation is most likely. Flow separation also enhances energy dissipation due to increased velocities, resulting in greater loss of tidal energy and weakened stratification. Flow separation and the associated drag increase are expected to be more common in meanders of tidal channels than rivers, where point bars that inhibit flow separation are more commonly found. The increased drag due to flow separation affects the tidal amplitude and phasing along the estuary and creates potential morphological feedbacks.

## 1 Introduction

### 1.1 Sinuous tidal channels

Rivers often have sinuous planforms (Langbein and Leopold, 1966). The natural processes that shape the sinuous form of river channels result from interactions between the fluid motion that carries sediment (e.g. along-channel flow and secondary circulation in a cross-sectional plane) and the erosion and deposition at the bed (Langbein and

22 Leopold, 1970; Seminara, 2006). In coastal systems, estuarine channels often inherit the sinuous geometry of river  
23 channels as sea level rises and drowns the fluvial channel (Fagherazzi et al., 2004).

24 Channel curvature can cause secondary circulation in a lateral plane perpendicular to the flow direction, as a  
25 result of the local imbalance between the centrifugal acceleration and barotropic pressure gradient in the vertical  
26 (Thomson, 1877). Secondary circulation has been predicted by the analytical solution presented by Rozovskii  
27 (1957) and Kalkwijk and Booij (1986), and observed in both rivers (e.g. Apmann, 1964) and tidal meanders (e.g.  
28 Seim and Gregg, 1997). This lateral circulation causes sediment transport across the channel and in turn provides  
29 feedbacks to meander morphology including erosion of outer bank, evolution of meander position, deposition at  
30 the inner bank, and growth of point bars. However, in curved estuarine channels, salinity stratification can suppress  
31 secondary circulation (e.g. Seim and Gregg, 1997) and the baroclinic pressure gradient can even reverse the sense  
32 of the lateral circulation compared to that expected for a river (e.g. Kranenburg et al., 2019). The differences in  
33 secondary circulation due to stratification and baroclinic forcing may contribute to the absence of point bars in  
34 some tidal meanders, which has consequences for the along-channel dynamics.

35 Channel curvature can also cause flow separation of the along-channel velocity at the inside of bends, which  
36 is observed at sharp channel bends in both rivers (e.g. Ferguson et al., 2003) and tidal channels (e.g. Leeder and  
37 Bridges, 1975). The bend sharpness is customarily quantified as  $R/w$ , the ratio of bend radius of curvature to  
38 channel width. Typical values of  $R/w$  are in the range of 1.5 – 4.3 for rivers (Leopold and Wolman, 1960) and  
39 1.6 – 5 for tidal channels (Marani et al., 2002), and the bends where flow separation occurs tend to be sharper  
40 than average, e.g.  $R/w < 1.5$  (examined more below). Flow separation can significantly impact flow structure  
41 in curved channels as well as increase along-channel drag (Leopold, 1960; James et al., 2001; Blanckaert, 2015),  
42 which will be examined in the following section.

## 43 **1.2 Increased drag coefficient in sinuous channels**

44 In shallow coastal systems, bottom friction is a major source of drag, and it typically scales with physical roughness  
45 elements of the bed (bottom roughness  $z_0$ ), whether grain size (Nikuradse, 1933) or bedforms (Grant and Madsen,  
46 1982). Friction is customarily represented with quadratic velocity and a dimensionless drag coefficient  $C_D$ .  $C_D$   
47 can be related to  $z_0$  and water depth by assuming a log-layer for near-bottom velocity.  $C_D$  is defined based on a  
48 reference velocity, usually taken at a fixed elevation (e.g., 1 m above the bed) or the depth-averaged velocity. A  
49 typical value for  $C_D$  of around 0.003 – 0.004 for shallow coastal and estuarine flows corresponds with a  $z_0 =$   
50 0.002 m for a reference velocity at 1 m above the bed or for depth-averaged flow for a water depth of 5 m. Other  
51 approaches to characterizing the effect of friction on open channel flow include Manning’s  $n$ , the Darcy Weisbach

52  $f$  and Chézy's  $C$  (James et al., 2001), but here we focus on the drag coefficient  $C_D$ .

53 In addition to bottom roughness, larger scale features can increase drag on the flow including coral reefs (e.g.  
54 Kunkel et al., 2006; Lentz et al., 2017; Rogers et al., 2018), vegetation (e.g. Kadlec, 1990; Nepf, 1999; Monismith  
55 et al., 2019) and form drag from topography (e.g. Warner and MacCready, 2014). This research will characterize  
56 a type of form drag, in particular on how channel meanders can increase the effective drag at larger scales. In this  
57 research,  $C_D$  is still defined based on quadratic velocity, but  $C_D$  quantifies the total drag instead of only bottom  
58 roughness. An example of form drag in a tidal flow was found for a headland in Puget Sound, where McCabe et al.  
59 (2006) and Warner and MacCready (2014) investigated the enhanced friction due to flow separation and internal  
60 wave generation.

61 Increased drag in sinuous channels compared with straight channels has been noted previously. In laboratory  
62 experiments with a sinuous channel, increased flow resistance and excess energy dissipation were observed around  
63 the bend (Leopold, 1960). In natural streams, meandering channels have been found to have Manning's  $n$  values as  
64 much as 30% greater than similar straight channels (Chow, 1959), and Arcement and Schneider (1989) suggested  
65 modifications to Manning's  $n$  to account for the increased drag in meandering rivers. Most of the examples of  
66 enhanced drag due to meanders are from rivers, but observations from a marsh also found increased surface slope  
67 in the midreach of a sharply sinuous channel (Leopold et al., 1993), suggesting that the sharp bends may have  
68 contributed to the enhanced drag and increased Manning's  $n$ .

69 Several processes have been suggested as potentially contributing to enhanced drag with channel curvature,  
70 including dissipation in hydraulic jumps at high Froude number  $F_r$  (Leopold, 1960), extra bottom stress from  
71 lateral circulation (Chang, 1984), and form drag from flow separation (James et al., 2001). In tidal channels,  $F_r$  is  
72 usually relatively low, so hydraulic jumps are unlikely to be a major factor. Lateral circulation, that is generated  
73 by the centrifugal acceleration of flow around bends and potential interactions with the salinity field, can enhance  
74 near-bed velocities and increase bottom stress and turbulent dissipation. Flow separation, in which streamlines of  
75 the along-channel flow detach from the channel bank and lead to a separation zone, has been observed in natural  
76 meanders, headlands and islands (e.g. Leeder and Bridges, 1975; Wolanski et al., 1984; Signell and Geyer, 1991).  
77 Flow separation creates a low-pressure zone behind the separation point and generates vortices from the boundary  
78 layer that are injected into the interior flow (Signell and Geyer, 1991). Flow separation in sinuous channels has  
79 been studied through laboratory measurements and observations. Lee eddies were observed in sinuous open channel  
80 experiments with relatively high mean velocity and strong curvature, causing the deformation of the free surface  
81 and restricting the flow to a narrower part of the cross-section (Leopold, 1960). Inner bank separation and its  
82 influence on the flow structure were reported by Blanckaert (2011) and Blanckaert (2015) in sharp bend flume

83 experiments. In natural tidal channels, Leeder and Bridges (1975) noted in the Solway Firth that flow separation  
84 effectively decreased the width and increased the local velocity, and suggested that flow separation is to be expected  
85 in many natural systems. The formation of counter-rotating eddies near the apex of bends was reported by Seim  
86 et al. (2006) in the Satilla River estuary, and noted to have similarities with flow around headlands as in  
87 Signell and Geyer (1991). Flow separation in the lee of a bend and weak fluid recirculation in the separation zone  
88 were also observed in rivers, including the Embarras River (Frothingham and Rhoads, 2003) and the River Dean  
89 (Ferguson et al., 2003).

90 Although flow separation in sinuous channels has been widely observed, the influence of flow separation on  
91 resistance and drag remains mostly conceptual. James et al. (2001) investigated the drag increase associated with  
92 flow separation in laboratory sinuous channels and reported that vegetation can decrease drag compared to an  
93 unvegetated sinuous channel by reducing separation at sharp bend. James et al. (2001) showed the dependence of  
94 Manning’s  $n$  on the curvature ratio (the centerline radius of the bend to the effective channel width) in unvegetated  
95 channels, but with limited physical explanation. Blanckaert (2015) noted the dependence of flow separation on  
96  $H/w$  and the curvature ratio  $R/w$ , but did not examine in detail the influence of these parameter on the drag.  
97 Leopold (1960) proposed that hydraulic jumps in the zone of curvature reversal can explain the energy loss and  
98 increased flow resistance, but the flow in tidal channels rarely has sufficiently high  $F_r$  for this mechanism to apply.

### 99 1.3 Overview

100 In this project, we built idealized numerical models motivated by observations from the North River estuary (MA,  
101 USA) to explore the basic processes that leads to increased drag in sinuous channels. Field studies were conducted  
102 in the North River estuary, a sinuous tidal channel through salt marsh that discharges into Massachusetts Bay  
103 (Kranenburg et al., 2019). The North River has relatively large tides (2 – 3.5 m range) and modest river discharge  
104 (typically  $< 5 \text{ m}^3/\text{s}$  except for brief events of  $10 - 40 \text{ m}^3/\text{s}$ ), so stratification is weak and intermittent. The channel  
105 aspect ratio (channel width to depth,  $w/H$ ) in the North River is about 10, and the bends are relatively sharp with  
106 the smallest  $R/w$  being 1.2. Measurements of velocity and pressure gradient on the North River resulted in a  
107 depth-averaged velocity drag coefficient  $C_D$  of  $0.005 - 0.01$  during ebb tide and  $0.01 - 0.02$  during flood tide  
108 (Kranenburg et al., 2017). However, typical values for estuaries with similar bottom roughness and water depth are  
109 in the range of  $0.002 - 0.005$  (e.g. Li et al., 2004). In the North River, local measurements of velocity and near-bed  
110 stress based on the turbulence spectra yielded a drag coefficient of 0.003 in this expected range (Kranenburg et al.,  
111 2019), in sharp contrast to the  $C_D$  based on the pressure gradient that was greater by a factor of 2 to 7.

112 Through an idealized numerical model study scaled based on these observations, we examine the mechanisms

by which flow separation in sharp sinuous channel bends increase drag and energy dissipation. In section 2, we introduce the numerical model setup. Section 3 shows the effects of channel curvature on drag and tidal propagation, and investigates the increased drag and energy dissipation associated with flow separation. In section 4, we summarize numerical results and show the dependence of this increased drag coefficient on channel geometry. In section 5 we introduce a theoretical flow separation model to explain the parameter dependence and compare with our numerical results and other previous research. In section 6, we discuss the influences of flow separation and the increased drag coefficient on sinuous channel dynamics as well as the broader application of the results, including comparison of rivers and tidal channels. Section 7 is a conclusion.

## 2 Model setup

We applied the the Regional Ocean Modeling System (ROMS) (Shchepetkin and McWilliams, 2005; Haidvogel et al., 2008; Warner et al., 2010) for the idealized sinuous estuary channel modeling. The grid is structured, with high resolution in the sinuous region at the center of model domain and increasing grid spacing toward the open ocean boundaries and the upstream river boundary. A stretched, terrain-following coordinate is used in the vertical direction. The estuary model has semi-diurnal tides imposed onto the open ocean boundaries with a 12-hour period, with a sinusoidal water level of 1 m amplitude and velocity of 0.5 m/s. A constant river discharge of  $5 \text{ m}^3/\text{s}$  is input at the upstream boundary, corresponding to a mean velocity of 1 cm/s in the upper channel and 0.5 cm/s in the sinuous channel near the estuary mouth. Salinity is 32 on the open ocean boundaries and 0 on the river boundary, and it is initialized as a linear decrease from the shelf into the estuary. Temperature is uniform throughout the entire domain. The model was run for a 20-day period, i.e. 40 tidal cycles, to ensure that a quasi-steady state was reached. Model analysis was based on the last two tidal cycles. The generic length-scale (GLS) mixing scheme is used for the vertical turbulent mixing (Umlauf and Burchard, 2003; Warner et al., 2005) and the horizontal mixing coefficient  $K_H$  is set to  $0.01 \text{ m}^2/\text{s}$ . Bottom roughness  $z_0$  is 0.002 m, a typical value for a bed with ripples (Grant and Madsen, 1982).

The shelf is 40-km long and 14-km wide, with depth linearly decreasing from 100 m to 7 m toward the coast. A narrow tidal inlet (700-m wide) is located at the estuary mouth, followed by a lagoon with a channel (400-m wide) in the middle and shallow flats on the side. The channel exponentially converges landwards until 6.5-km into the estuary, and after that the channel is uniform width  $w = 200 \text{ m}$ , with 20 grid cells across the channel. The sinuous region is located between 6.5 and 19-km, and the total along-channel length is approximately 40 km. Channel thalweg depth linearly decreases from 7 m at the mouth to 3 m at 22 km, with a slope of  $\sim 0.18 \text{ m/km}$ ,

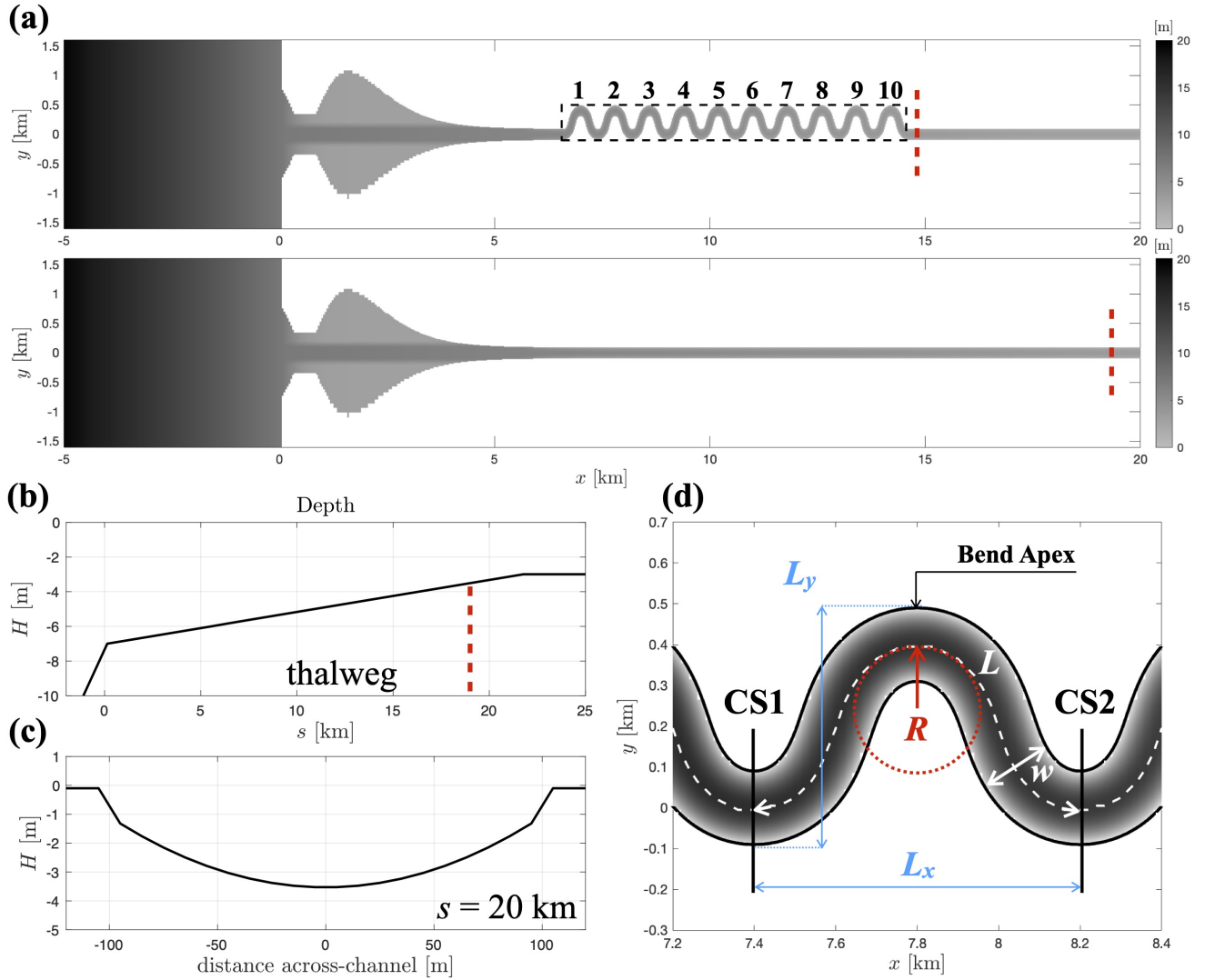


Figure 1: (a): Model bathymetry of the idealized sinuous and straight channel estuaries. Only the center parts of the model grids are shown. The estuary starts from  $x = 0$  and  $x < 0$  is the shelf. The sinuous region is marked by dashed black lines. Channel bends are numbered as 1 – 10. (b): Depth of the channel thalweg as a function of along-channel distance  $s$ . (c): Cross-sectional bathymetry at  $s = 20$  km, corresponding to the cross-section denoted by the dashed red lines in panels (a) and (b). (d): Geometric parameters of channel bend 2.  $L_x$  is the Cartesian length;  $L_y$  is the Cartesian width;  $L$  is the along-channel length.  $R$  is the minimum radius of curvature of the channel centerline along the bend.  $w$  is the channel width. Black lines mark the position of cross-sections (CS1, CS2) used in the following model analysis.

and the thalweg depth is a uniform 3 m from 22 km to the landward boundary (Figure 1 (b)). The channel has a parabolic cross-sectional profile with a minimum depth of 1.5 m to ensure that the bed does not emerge at low tide (Figure 1 (c)). The sinuous channel shape is created following the form of sine-generated functions (Langbein and Leopold, 1970), and the mathematical expression is shown in Appendix A. The sinuous region is composed of ten continuous  $144^\circ$  bends, numbered in Figure 1 (a), where we are focusing on just half the bends to limit redundancy. The minimum radius of curvature (of the channel centerline) is 164 m at the bend apex. The Cartesian length of

each channel bend is 800 m and the Cartesian width is 600 m; the along-channel length of each bend is 1240 m (Figure 1 (d)).

A straight channel model is used as a comparison of the sinuous channel model. The grid, boundary conditions, channel width, depth, bottom slope and lateral bathymetric profile are exactly the same in the two models and the only difference lies in the channel planform. The total along-channel length is also the same to make the total volume of the two estuaries identical.

Additional model grids with different sinuous channel shapes are used to explore parameter space in section 4, but the overall structure is similar for the other cases. The channel aspect ratio varies between 10 and 60, which covers a wide range of salt marshes, tidal flats and rivers, and the  $R/w$  (bend sharpness) ranges between 0.7 – 1.6. Both the field study and numerical experiments focus on channel bends that are relatively sharp for rivers and tidal meanders (Leopold and Wolman, 1960; Marani et al., 2002) but are within the range commonly found in nature (e.g. Nanson, 2010; Schnauder and Sukhodolov, 2012; Marani et al., 2002).

### 3 Numerical model results

In this section, we analyze model results and explore the underlying physics that cause the increased drag in meanders. In section 3.1, we compare drag coefficients between the sinuous and straight estuary models. In section 3.2, we examine the effects of the increased drag with channel curvature on tides and stratification. In section 3.3, we characterize flow separation and the form drag. In section 3.4, we calculate the energy budget and show how flow separation increases energy dissipation.

#### 3.1 Increased drag coefficient in meanders

It is customary to write drag force as

$$\tau = \rho C_D \bar{u} |\bar{u}|, \quad (1)$$

where  $\tau$  is the total drag force, including bottom stress and other sources of drag.  $\rho$  is density,  $C_D$  is the drag coefficient and  $\bar{u}$  is a reference velocity, often taken as the depth-averaged velocity or the velocity at a fixed elevation above the bottom.

The drag coefficient is used to represent resistance in the along-channel momentum equation

$$\frac{\partial U}{\partial t} + U \frac{\partial U}{\partial s} = -g \frac{\partial \eta}{\partial s} - \frac{1}{2} \beta g \frac{\partial \bar{S}}{\partial s} H - C_D \frac{U |U|}{H}, \quad (2)$$



where  $U$  is the cross-sectionally averaged streamwise velocity and  $\bar{S}$  is the cross-sectionally averaged salinity.  $\eta$  and  $H$  are the laterally averaged water level and water depth.  $\beta$  is the haline contraction coefficient. Local (depth-averaged) velocity, water level, salinity are often all that can be measured in field observations, but here we used the cross-sectional average of all the properties because of the large lateral variations in these quantities in the sinuous channel case. The advection term associated with cross-stream velocity is neglected in cross-sectionally averaged momentum budget because it is small. We can calculate an effective  $C_D$  that satisfies the momentum budget

$$C_D = \left( \frac{\partial U}{\partial t} + g \frac{\partial \eta}{\partial s} + \frac{1}{2} \beta g \frac{\partial \bar{S}}{\partial s} H + U \frac{\partial U}{\partial s} \right) / \left( \frac{-U|U|}{H} \right). \quad (3)$$

We calculated the effective drag coefficient across the bend between sections CS1 and CS2 over a tidal cycle using (3). Only the bend-scale drag coefficient is calculated because form drag is usually defined as a spatial integral over the topography of interest (McCabe et al., 2006). The drag coefficient in the straight model is evaluated at locations with same along-channel distance. Data points near slack water are removed to avoid very small values in the denominator of (3). In both models, the water level gradient is the dominant term, and the unsteady, advective, and baroclinic terms are at least an order of magnitude smaller.

Model results show that the drag coefficient in the sinuous estuary is two to four times larger than the straight estuary, e.g. 0.006 – 0.015 compared to 0.003 – 0.004. The models are identical except for the channel meanders, suggesting that this increase in drag by a factor of 2 – 4 is associated with the sinuous planform.  $C_D$  is averaged over flood and ebb tide separately in both models (Figure 2). In the straight model,  $C_D$  is slightly larger during ebb tide than flood tide, but differences are small. In the sinuous channel, the drag coefficient is larger during flood tides than ebb tides, which is related to variations in water depth and will be discussed in section 4. The drag coefficient also shows temporal fluctuations during flood tides due to instability in the flow field (section 3.3), so the maximum  $C_D$  (e.g.  $\sim 0.015$  in bend 1-3) is larger than the temporal average  $C_D$  (e.g.  $\sim 0.012$  in bend 1-3) in Figure 2. Both the magnitude of the drag coefficient in the sinuous channel and the flood-ebb asymmetry are broadly consistent with field observations from the North River, on which the model grid was scaled (Kranenburg et al., 2017).

In the sinuous region, the drag coefficient is significantly larger than that of the straight model, while outside the sinuous region the drag coefficient decreases. The drag coefficients also have different along-channel trends in the two models. The drag coefficient in the straight model increases landwards, while in the sinuous model  $C_D$  has a decreasing trend. These opposite behaviors will be explained in section 4. As a result, difference between the sinuous and straight models is greatest in the seaward bends, and we have focused the subsequent analyses on bend 2.

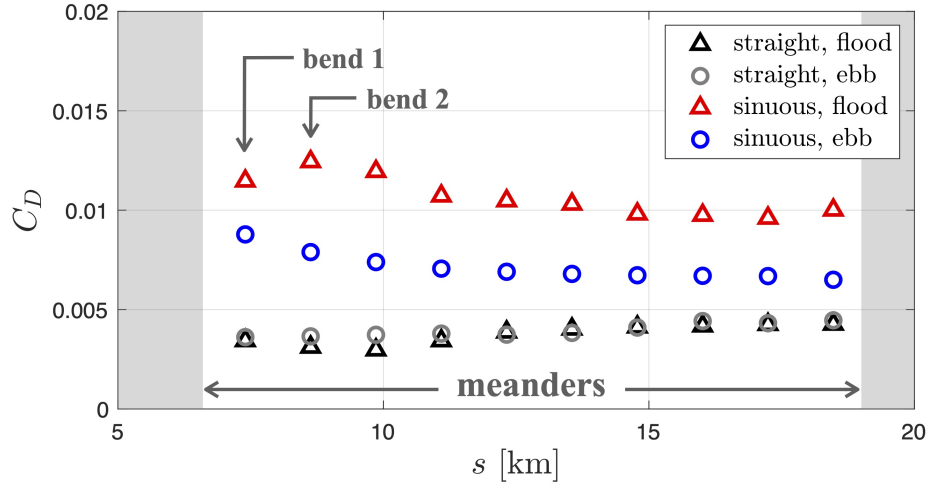


Figure 2: Drag coefficient as a function of along-channel distance.  $C_D$  is averaged over flood and ebb tide separately in both the straight and sinuous model. The black triangles and gray circles represent flood and ebb tide respectively in the straight model; the red triangles and blue circles represent flood and ebb tide in the sinuous model. The white background shows the range of meanders (the sinuous region) and the arrows mark the first two bends as a representative.

### 3.2 Along-channel change of tides and stratification

In shallow estuaries or inlet systems, the drag directly affects tidal propagation, including tidal amplitude decay and phase lag with distance along the estuary (e.g. Aubrey and Speer, 1985). The increased drag in tidal meanders can therefore have important influences on the water level change in estuaries, which impacts coastal flooding and marsh resilience. Harmonic analysis is employed to examine the influences of meanders on tidal elevation. The numerical system is forced by a 12-hour semi-diurnal tide, so in the harmonic analysis, M2 (12-hour) tide and M4 (6-hour) and M6 (4-hour) overtides are selected as three major tidal components for least-squares fitting.

The amplitude and phase of the dominant M2 tide is shown in Figure 3. In the straight model, the amplitude of M2 tide decays as it propagates into the estuary until being reflected near the upstream river boundary. The decay rate is  $\sim 0.024$  m/km, which is mainly attributed to frictional dissipation. The sinuous model shows a faster tidal amplitude decay ( $\sim 0.040$  m/km) than the straight model, which indicates a greater energy loss (discussed in section 3.4). Also, the M2 tidal phase lag is greater in the sinuous channel than the straight channel, as is expected from the increased effective drag (Aubrey and Speer, 1985).

Comparison of tidal elevation in the two models demonstrates that meanders can affect tidal water levels in the landward parts of the estuary. Meanders also can impact the growth of overtides and tidal asymmetries. The ratio of amplitudes M4/M2 is similar in the two models but M6/M2 is larger in the sinuous model than the straight model by almost a factor of 2, which indicates greater non-linearity with the sinuous channel.

The cross-sectionally averaged velocity  $U$  is less in the sinuous channel than the straight, which is in agreement

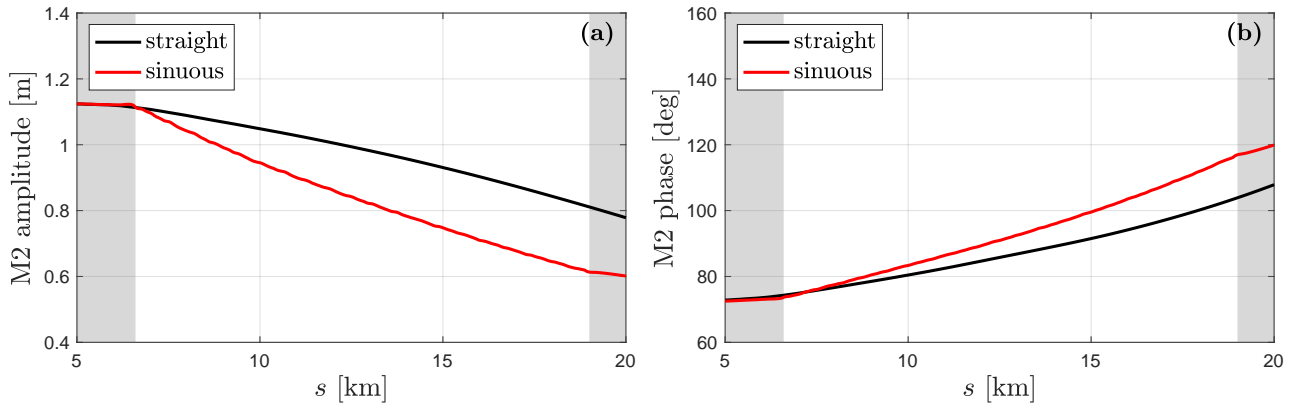


Figure 3: (a): M2 tidal amplitude along the channel. (b): M2 tidal phase along the channel. Red lines represent the sinuous model and black lines represent the straight model. The white background shows the range of the sinuous region.

with the tidal amplitude decay in Figure 3. Decreased tidal amplitude indicates smaller estuary volume change associated with tidal fluctuations, and as a result, smaller volumetric flux and weaker cross-sectional average current. However, despite the weaker cross-sectionally averaged velocity, the maximum local velocities in the sinuous channel exceed those in the straight channel by up to 30%. This result suggests stronger lateral variations in the velocity field because of channel bends, which will be further investigated in section 3.3.

Differences in stratification are also apparent between the sinuous and straight channel cases. In both cases, the tidally averaged  $\Delta S$  (difference between surface and bottom salinity) is less than 6 psu, relatively weak stratification that is consistent with the strong tidal currents and small river discharge. However, the sinuous model has a smaller tidally averaged  $\Delta S$  than the straight channel, indicating weaker stratification due to the existence of channel bends. The mechanism of how sinuous channels decrease stratification is still unclear, and could be related to secondary circulation in the bend or flow separation near the bend apex, and this will be discussed in section 3.4.

### 3.3 Flow separation and form drag

Flow separation can generate recirculating eddies near the inner bank and produce a “dead zone” or “separation zone” in the lee of channel bends (e.g. Rozovskii, 1957; Ferguson et al., 2003; Blanckaert, 2011), which narrows the effective flow width and increases the local velocity (Leopold, 1960; Leeder and Bridges, 1975). Although outer bank separation is also observed in some channel bends (e.g. Blanckaert et al., 2013), the present research focuses on separation at the inner bank where flow is reversed as a result of an adverse pressure gradient. The lateral profile of velocity becomes deflected away from the inner bank and the separation zone grows from near the bend apex toward the lee of bend.

Flow separation is seen in model results at both maximum flood and maximum ebb, as illustrated by the maps

of water level and depth averaged velocity at maximum flood (Figure 4 (a)). The boundary of the separation zone is represented by the deflection points in the velocity profiles. Streamlines at maximum flood are also displayed in Figure 4 (a), with a recirculating eddy in the lee of the channel bend. Free surface deformation is observed in the lee of bend, which is related to the formation of recirculating lee eddies (Leopold, 1960). Water level field can be regarded as the depth averaged barotropic pressure field. A sudden pressure drop occurs near the boundary of the separation zone and a low pressure zone is located downstream of the bend. This pressure drop creates an extra “form drag” or “pressure drag”, that increases the drag coefficient. Flow separation also increases instability in the velocity field, which is reflected in temporal fluctuations in  $C_D$ .

The separation zone decreases the main flow width and consequently increases the main flow velocity outside the separation zone. We define an effective width for the main flow due to the expansion of flow separation into the channel, as illustrated in Figure 4 (b). The effective main flow region is defined by  $\bar{u} > 0.5U$ , with  $\bar{u}$  being the local depth averaged streamwise velocity and  $U$  being the cross-sectionally averaged streamwise velocity. The effective width is decreased by  $\sim 20\% - 30\%$  in the sinuous channel because of flow separation, while in the straight channel, the effective width is equal to the channel width. Along-channel momentum is more concentrated into a narrower main flow region in the sinuous channel and maximum velocity is intensified as a result of effective width decrease, which explains why the maximum velocity is greater in the sinuous model despite lower cross-sectional average velocities than the straight model (section 3.2).

The evolution of velocity field during early flood tide illustrates flow separation (Figure 4 (c)). During early flood prior to flow separation, flow is attached to the inner bank with the maximum streamwise velocity near the inside of the bend. This is common in flat bottom channel flow in the laboratory (e.g. Blanckaert, 2015) and natural meanders without a point bar (e.g. Kranenburg et al., 2019), and will be theoretically explained in section 5. Flow near the inner bank is decelerated after passing the bend apex because of the adverse pressure gradient set by channel curvature. As the tidal current grows, this adverse pressure gradient is strengthened and velocity near the inner bank keeps decreasing. Flow separation occurs when the main flow detaches from the inner bank. The maximum velocity increases as the effective width of the main flow decreases, with the the velocity maximum separated from the inner bank and shifted toward the centerline (also see Kranenburg et al. (2019) Fig. 7). Flow near the inner bank can slow to zero or reverse as the flow separation evolves, which leads to the formation of recirculating eddies.

Lateral water level variations are also increased as flood tide and flow separation grows (Figure 4 (c)). This water level difference sets up a cross-channel barotropic pressure gradient, which generates the “normal” secondary circulation for homogeneous flow around a bend. Lateral salinity differences can instead create lateral baroclinic

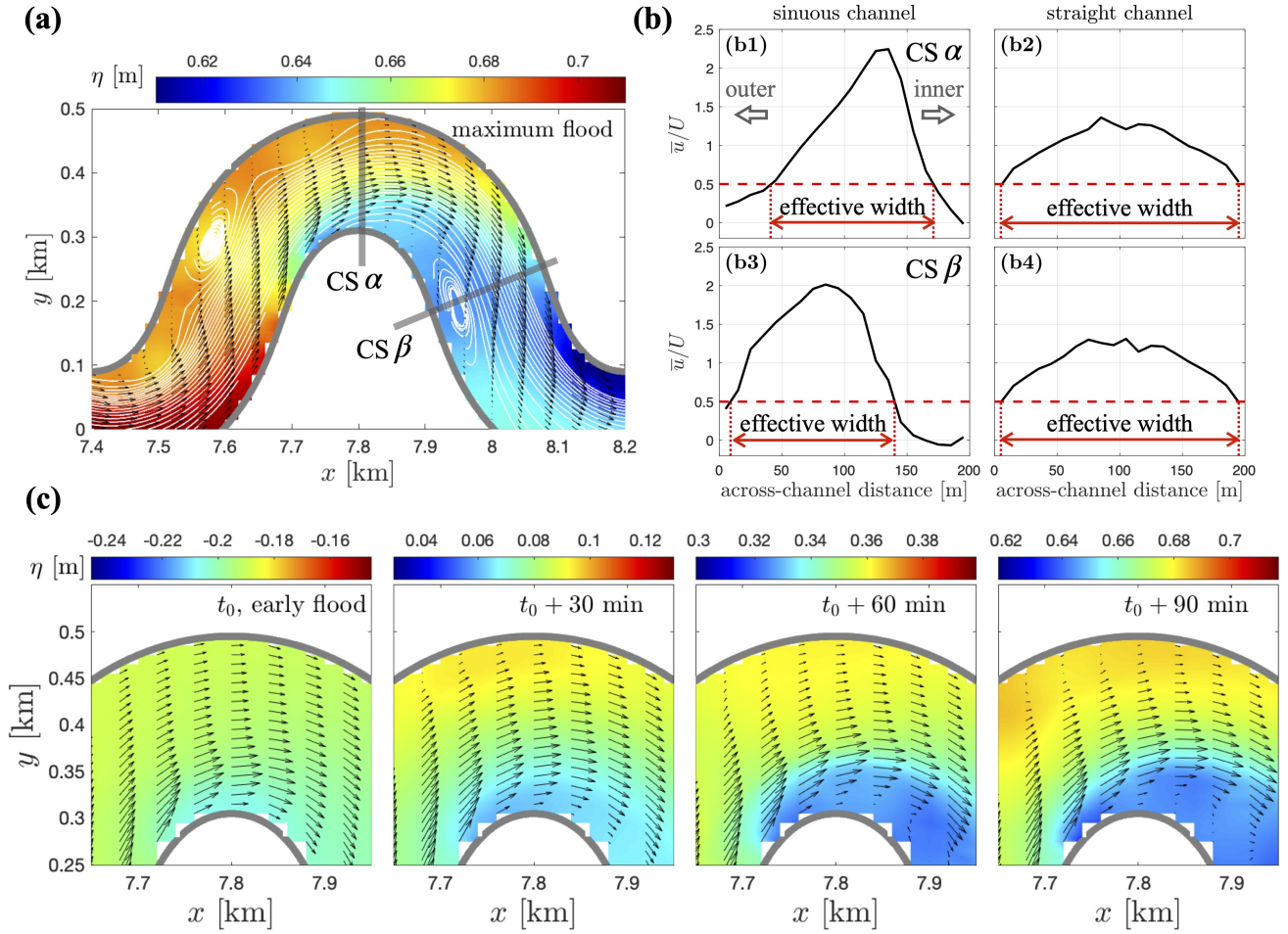


Figure 4: **(a)**: Water level, streamlines and velocity field of channel bend 2 at maximum flood tide. White lines show streamlines, including the main flow and the recirculating eddy in the lee of bend 2. Black arrows show the depth averaged velocity. Gray lines represent the river banks. **(b)**: Lateral profile of streamwise velocity scaled by local cross-sectional average velocity at two cross-sections in the sinuous channel and the same along-channel distance locations in the straight channel. The inner bank is on the right side of the graph. Effective channel width is defined as the lateral length of where  $\bar{u} > 0.5U$ , in which  $\bar{u}$  is the local depth-averaged streamwise velocity and  $U$  is the cross-sectionally averaged streamwise velocity. **(b1)** and **(b3)** correspond to cross-sections  $CS\alpha$  and  $CS\beta$  in panel **(a)**, respectively. **(b2)** and **(b4)** show locations with the same along-channel distance in the straight channel. **(c)**: Evolution of flow field near the bend apex, with snapshots of four different times during early flood tide. The colormap shows the waterlevel. The range of the colormap varies as water level grows during early flood but the span of the colormap is the same in all the small panels.  $t_0$  is early flood tide and  $t_0 + 90$  min is maximum flood tide.

pressure gradients that force lateral circulation that is reversed from the normal homogeneous secondary circulation (e.g. Kranenburg et al., 2019). Both the normal secondary circulation and the reversed circulation are observed in our numerical models, as a result of spatial and temporal variations in the balance among the cross-channel barotropic pressure gradient, baroclinic pressure gradient and centrifugal force.

To quantify the form drag contribution directly, we write the integral form of the momentum equation (McCabe

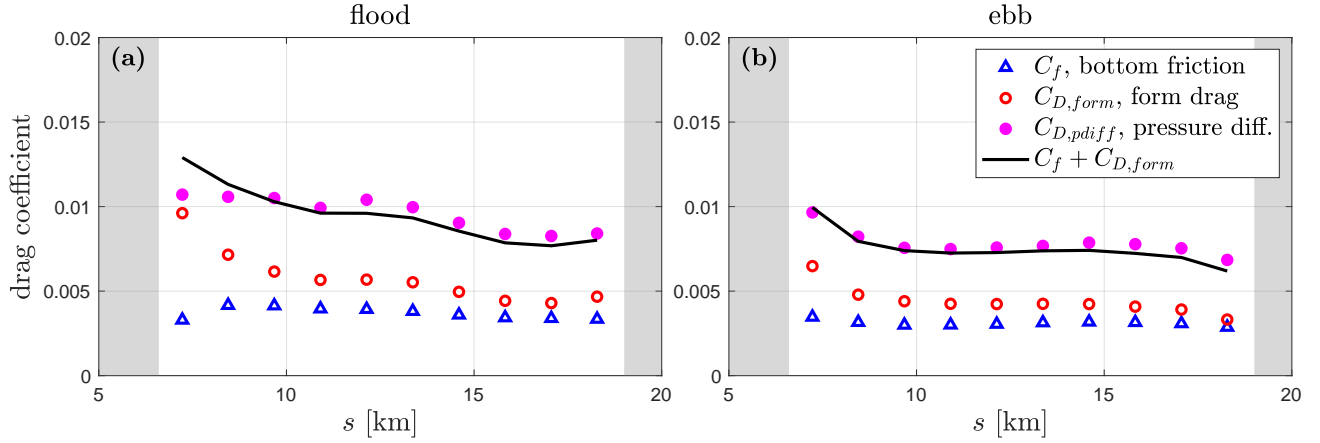


Figure 5: Drag coefficients corresponding to different terms of momentum loss. **(a)**: maximum flood tide. **(b)**: maximum ebb tide. Magenta dots represent the pressure difference around each bend; red circles represent the form drag; blue triangles represent bottom friction. Black lines are the sum of bottom friction and form drag, i.e. the total drag. All the terms are calculated or integrated over channel bend scale, and converted into corresponding drag coefficients. The white background shows the range of the sinuous region.

et al., 2006) over each bend as

$$\frac{\partial}{\partial t} \int_V \rho_0 u dV + \int_{A_{CS1}+A_{CS2}} \rho_0 u \vec{u} \cdot \vec{n} dS = \int_{A_{CS1}} p dS - \int_{A_{CS2}} p dS + \int_{A_w+A_b} p \xi_x dS + \int_{A_b} \tau_{bx} dS, \quad (4)$$

where  $\xi_x$  corresponds to the projection in  $x$ -direction.  $A_{CS1}$  and  $A_{CS2}$  represent the cross-sectional areas at each end of the control volume; and  $A_w$  and  $A_b$  represent the areas of the vertical sidewalls and channel bed. The momentum budget is calculated at maximum flood and maximum ebb. The unsteady and advection terms on the left side of (4) are small, so the momentum budget in  $x$ -direction results primarily from the pressure difference between the two cross-section ends (first two terms on the right side of (4)), the form drag (third term) and the bottom friction (last term), as there is no friction on the surface or sidewalls of our model. Baroclinic effects are also small (section 3.1) so only the barotropic pressure is included in this calculation.

In the straight model, the pressure difference between the ends of the control volume is balanced by bottom friction, and there is no form drag due to the channel geometry (Appendix B). The decreasing thalweg depth along the channel also creates a large pressure force between the ends of the control volume that is balanced by the bottom slope, and we have removed this bottom-slope effect in calculating the momentum budget to focus on the pressure force and form drag associated with water level (Appendix B). In the sinuous model, the right-side terms in (4) are calculated over each bend and converted into corresponding drag coefficients based on the cross-sectional average velocity (Figure 5).  $C_{D,pdiff}$ ,  $C_{D,form}$  and  $C_f$  correspond to the pressure difference, form drag and bottom friction respectively. The drag in Figure 5 is calculated slightly differently from that in Figure 2 — Figure 2 shows

the temporal average while Figure 5 uses snapshots at maximum flood and maximum ebb — but the results are consistent. The bottom friction in the sinuous channel is similar to the straight channel, e.g.  $C_f \sim 0.003 - 0.004$ . The pressure difference (total drag) is a factor of  $\sim 2 - 3$  larger than bottom friction in the sinuous channel, indicating there is another source of momentum loss, i.e. the form drag associated with flow separation. Integration of the sidewall and channel bed pressure (projected in the  $x$ -direction) directly represents the effect of the form drag on the momentum budget, and shows that it is up to a factor of 2 larger than bottom friction, and the momentum budget closes only when the pressure difference is balanced by the combination of bottom friction and form drag.

### 3.4 Energy dissipation

Flow separation not only causes an extra momentum loss by creating form drag, but also leads to a larger energy dissipation in the sinuous channel. The integral form of the energy equation (Gill, 1982; Zhong and Li, 2006) for horizontal velocities is

$$\begin{aligned} \int_{ACS} \left( p + \rho_0 \frac{u^2 + v^2}{2} \right) \vec{u} \cdot \vec{n} dS = & - \int_{A_b} \vec{u}_b \cdot \vec{\tau}_b dS - \int_V \rho_0 K_V \left[ \left( \frac{\partial u}{\partial z} \right)^2 + \left( \frac{\partial v}{\partial z} \right)^2 \right] dV \\ & - \int_V \rho_0 K_H \left[ \left( \frac{\partial u}{\partial x} \right)^2 + \left( \frac{\partial u}{\partial y} \right)^2 + \left( \frac{\partial v}{\partial x} \right)^2 + \left( \frac{\partial v}{\partial y} \right)^2 \right] dV. \end{aligned} \quad (5)$$

The left side is the net energy flux and the unsteady term is neglected as we have focused on tidally averaged energy balance. The right side is energy dissipation, which is composed of three parts: energy loss due to bottom shear stress  $\epsilon_b$  (the surface and sidewall stress are zero in our models), vertical turbulent dissipation  $\epsilon_v$  (the vertical viscosity  $K_V$  is set by the turbulence closure) and horizontal dissipation  $\epsilon_h$  (the horizontal viscosity  $K_H = 0.01 \text{ m}^2/\text{s}$ ). Energy flux and the three dissipation terms in the energy budget are calculated along the channel and converted to depth-integrated and laterally-averaged results (Figure 6).

In both the straight and sinuous models, the energy flux loss is generally balanced by the calculated total dissipation, which demonstrates that the energy budget closes in the models and numerical dissipation is negligible. Comparing the two models, we found that there is a larger energy loss in the sinuous model (Figure 6), which is consistent with the greater rate of decrease in tidal amplitude in section 3.2. The maximum dissipation values in the sinuous model, and therefore maximum energy loss rates, occur near the bend apexes.

The larger energy loss induced by meanders is caused by both increased dissipation associated with bed stress and enhanced vertical dissipation by turbulence. The bottom stress dissipation is larger in the sinuous model than the straight model, even though bottom stresses are similar in the two models (section 3.3). This can be explained by the decreased effective channel width due to flow separation near the bend apex, which accelerates the main

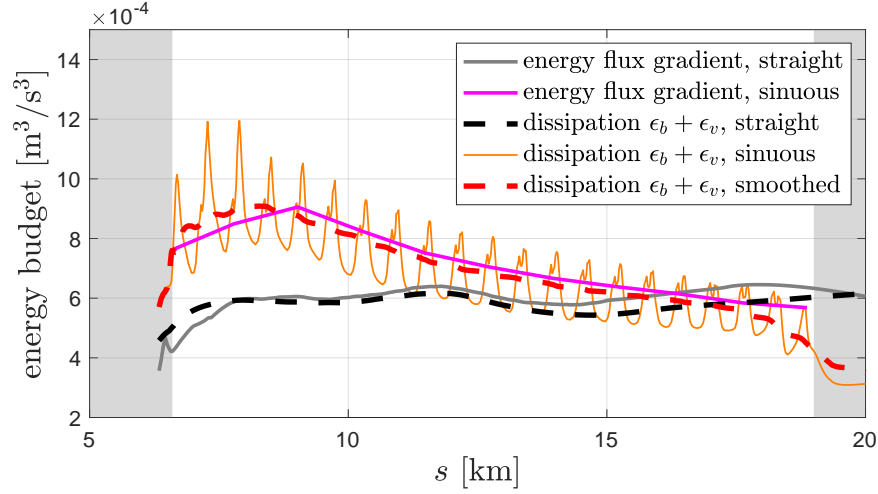


Figure 6: Terms in the energy budget in the sinuous and straight models as a function of along-channel distance. Solid gray and solid magenta lines represent the energy flux gradient in the straight channel and sinuous channel (evaluated at bend scale). Solid orange line: bottom dissipation  $\epsilon_b$  and vertical dissipation  $\epsilon_v$  in the sinuous channel. Dashed red line:  $\epsilon_b + \epsilon_v$  in the sinuous channel smoothed over bend scale. Dashed black line:  $\epsilon_b + \epsilon_v$  in the straight channel. The white background shows the range of the sinuous region.

316 flow because of continuity. Bottom dissipation can be estimated as

$$\epsilon_b = \tau_b u_b \sim \rho C_f \bar{u}^2 u_b, \quad (6)$$

317 where  $\tau_b$  is the bottom stress,  $u_b$  is the bottom velocity and  $\bar{u}$  is a reference velocity associated with the bottom  
 318 friction coefficient  $C_f$ . The cubic dependence of dissipation on velocity, together with the greater velocity near the  
 319 channel center due to flow separation, leads to a larger laterally averaged bottom stress dissipation in the sinuous  
 320 channel. There is also extra dissipation associated with lateral bottom shear stress and secondary circulation in  
 321 bends, but this is relatively small compared to the increased streamwise bottom stress dissipation.

322 The vertical turbulent dissipation depends on the vertical shear and vertical turbulent viscosity. Numerical re-  
 323 sults show that the vertical profile of streamwise velocity is more uniform in the sinuous model than the straight  
 324 channel, so there is less streamwise vertical shear. Although the vertical shear of cross-stream velocity is larger  
 325 in the sinuous model because of secondary circulation, the contribution to the total shear is small. However, the  
 326 vertical turbulent viscosity is increased in the sinuous model as a result of weaker stratification compared with the  
 327 straight channel. The source of this reduction in stratification and enhanced turbulence is still unclear, and it could  
 328 be associated with the accelerated streamwise velocities or the stronger secondary circulation. For comparison,  
 329 Nidzieko et al. (2009) found in a curved estuary channel that the destratification was caused by turbulent motions  
 330 rather than an overturning produced by lateral circulation. As with bottom dissipation, the vertical turbulent dissi-



331 pation scales with velocity cubed, so the increased turbulent dissipation in meanders also relates to the decreased  
332 effective channel width and velocity acceleration because of flow separation.

333 Horizontal dissipation also could contribute to the enhanced energy dissipation in the sinuous channel case.  
334 High vorticity fluid is generated near the inner bank due to the velocity shear set by the shallower bathymetry  
335 near the edges of the channel, and the high vorticity fluid can be injected into the center of the channel by flow  
336 separation, potentially increasing horizontal dissipation (e.g. Figure 8 (a), (c)). Signell and Geyer (1991) discussed  
337 similar processes of eddy formation around headlands and injection of high vorticity fluid from the boundary layer  
338 into the interior flow. However, although we observed greater horizontal dissipation in the sinuous channel than  
339 the straight channel, that term is still two orders of magnitude smaller than the bottom stress and vertical turbulent  
340 dissipation terms.

341 Previous investigations of the energy loss induced by sinuous channels proposed that the major sources of  
342 energy loss included increased bed friction from secondary circulation, increased turbulence induced by secondary  
343 circulation and turbulence in eddies associated with flow separation (e.g. James et al., 2001). However, our research  
344 suggests that the momentum redistribution caused by flow separation, i.e. decreased effective width and increased  
345 local streamwise velocity, is an important source of energy loss. These results are particularly relevant to tidal  
346 channels, which are shallower than most of the laboratory channels based on aspect ratio. For shallow systems,  
347 dissipation is primarily related to the bottom stress and vertical shear even though there is strong horizontal variation  
348 in velocity induced by the complex geometry.

## 349 **4 Parameter dependence of the drag coefficient**

### 350 **4.1 Parameter dependence on water depth**

351 For turbulent open channel flow with small roughness compared to the water depth, Lentz et al. (2017) proposed  
352 an estimate for the drag coefficient based on the depth-averaged velocity

$$C_D \approx \kappa^2 \left[ \log \left( \frac{H}{z_0} \right) + (\Pi - 1) \right]^{-2}, \quad (7)$$

353 in which  $z_0$  is the bottom roughness and  $H$  is the water depth.  $\Pi$  is Cole's wake strength and  $\Pi \approx 0.2$  for turbulent  
354 open channel flow (Nezu, 1993). In this formulation,  $C_D$  decreases as water depth increases, because velocity  
355 profile becomes less sheared in the upper water column with greater flow depth.

356 Results from the straight channel model show a decreasing trend with depth that is consistent with the theoretic-

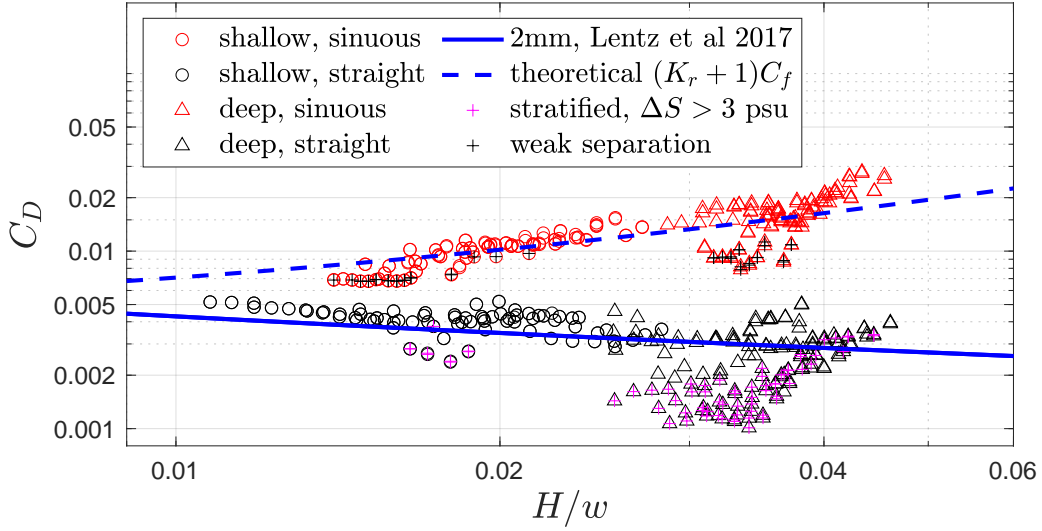


Figure 7: The drag coefficient as a function of  $H/w$ , with  $H$  being the laterally averaged water depth. Red circles: shallow sinuous model; red triangles: deep sinuous model; black circles: shallow straight model; black triangles: deep straight model. The solid blue line shows the  $C_D$  predicted by (7) with  $z_0 = 2$  mm. The dashed blue line shows the  $C_D$  predicted by (13) in section 5. The two shallow channel models were the original models employed in section 3 and the two deep channel models have the same channel shape as the shallow models and a depth of 7 – 12 m. In the straight model, stratified cases during ebb tide ( $\Delta S > 3$ ) are filled with magenta plus signs. In the sinuous model, weak flow separation cases (effective width  $> 0.9w$ ) are filled with black plus signs.

cal  $C_D$  in (7), as Figure 7 shows. The simulation results do not exactly match the theoretical result because we have parabolic channels instead of flat bottom channels, and the vertical velocity profile can be altered by stratification. In the straight model, the estuary is more stratified during ebb tide and these stratified cases ( $\Delta S > 3$ ) have a smaller drag coefficient than predicted by the formula, as are marked in Figure 7. The dependence of  $C_D$  in the straight channel is only on water depth  $H$  but not channel width  $w$ , which is different from the sinuous channel where  $C_D$  depends on both  $H$  and  $w$ . Although  $H$  is non-dimensionalized by  $w$  in our research,  $w$  is a constant in the models employed in Figure 7, so channel width does not affect the decreasing trend in the straight models.

In the sinuous channel models,  $C_D$  increases with the water depth scaled by channel width, which indicates a different dominant mechanism from the straight channel in exerting drag. Calculations of  $C_D$  are based on 1-hour averages to filter out fluctuations caused by instability associated with flow separation. As is discussed in section 3.3, flow separation is the major source of drag instead of bed friction. Therefore, the opposite depth dependence of  $C_D$  in sinuous channels is because flow separation is stronger in deeper water as it is less inhibited by bottom friction (or deeper water has relatively larger inertia), which thus leads to a larger momentum loss and a larger  $C_D$ . A quantitative explanation will be provided in section 5. Some weak flow separation cases are marked out in Figure 7, identified as bends where the effective width  $> 0.9w$  ( $w$  is channel width). These weak separation cases have relatively small drag coefficients, and occur only during ebb tide. The causes for this weak separation

are still unclear, and may depend on inhibition by the shallow bathymetry near the inner bank, greater stratification, or the secondary circulation.

The dependence on water depth explains the flood-ebb asymmetry in  $C_D$  (section 3.1). Water is deeper during flood tide because of the phase lag between water level and velocity, and as a result,  $C_D$  is larger during flood tide (section 3.1). Difference in water depth is the primary reason for this flood-ebb asymmetry, but differences in stratification and lateral circulation may also play a role. The increasing or decreasing trend of  $C_D$  as a function of along-channel distance (Figure 2) is also associated with its dependence on water depth. The channel model becomes shallower in the landward direction with a slope of  $\sim 0.18$  m/km (section 2), so the time-averaged  $C_D$  increases as water depth decreases landwards in the straight channel. On the contrary,  $C_D$  decreases landwards in the sinuous channel because  $C_D$  decreases as water depth decreases.

We chose channel width  $w$  to scale water depth  $H$  to follow the convention of other research on meanders, because the lateral circulation in meanders usually depends on  $H/w$  (reciprocal of aspect ratio). More importantly, unlike in straight channels in which  $C_D$  only depends on  $H$ ,  $C_D$  in sinuous channels depends on  $H/w$ . Blanckaert (2015) found that the width of flow separation zone primarily scales with the water depth, and consequently, changing the channel width alone can change the fraction of the channel affected by flow separation, and therefore affects  $C_D$ . The dependence on  $w$  is not shown above as the four models in Figure 7 have the same channel width, but cases with different channel widths will be examined in the following sections.

## 4.2 Parameter dependence on channel curvature

Previous research identified the dependence of flow separation and energy loss on bend sharpness, which is expressed as  $R/w$  with  $R$  being the bend radius of curvature and  $w$  being the channel width (e.g. Leopold, 1960; Leeder and Bridges, 1975). Although the mathematical model employed in that research was based on a hydraulic jump theory, which is different from our results (see section 5), their exploration of parameter space provides a useful framework. Other researchers have used the sinuosity (e.g. Arcement and Schneider, 1989), which is the ratio of the thalweg length to the straight line length in meanders, but James (1994) proposed that bend losses are not caused by sinuosity per se, but rather by the curvature of bend. In this research, we also chose bend sharpness as the geometric parameter to describe the effect of meanders on the flow.

Bagnold (1960) argued that the overall resistance in a sinuous channel should increase with decreasing curvature ratio  $R/w$ . An adjusted Manning's  $n$  that decreases with the curvature ratio was brought forward by James et al. (2001) from a flume experiment, consistent with the idea that the drag increases as bends become sharper. Blanckaert (2015) proposed several dominant geometry parameters controlling flow separation including  $R/w$ ,

where  $R$  is the minimum radius of curvature along the channel, and decreased  $R/w$  leads to stronger flow separation and thus a larger drag. Natural meanders usually show a variation in radius of curvature with a minimum at the bend apexes (e.g. Parsons, 2003), so in this research, we used the minimum centerline radius of curvature to define  $R/w$  and quantify bend sharpness.

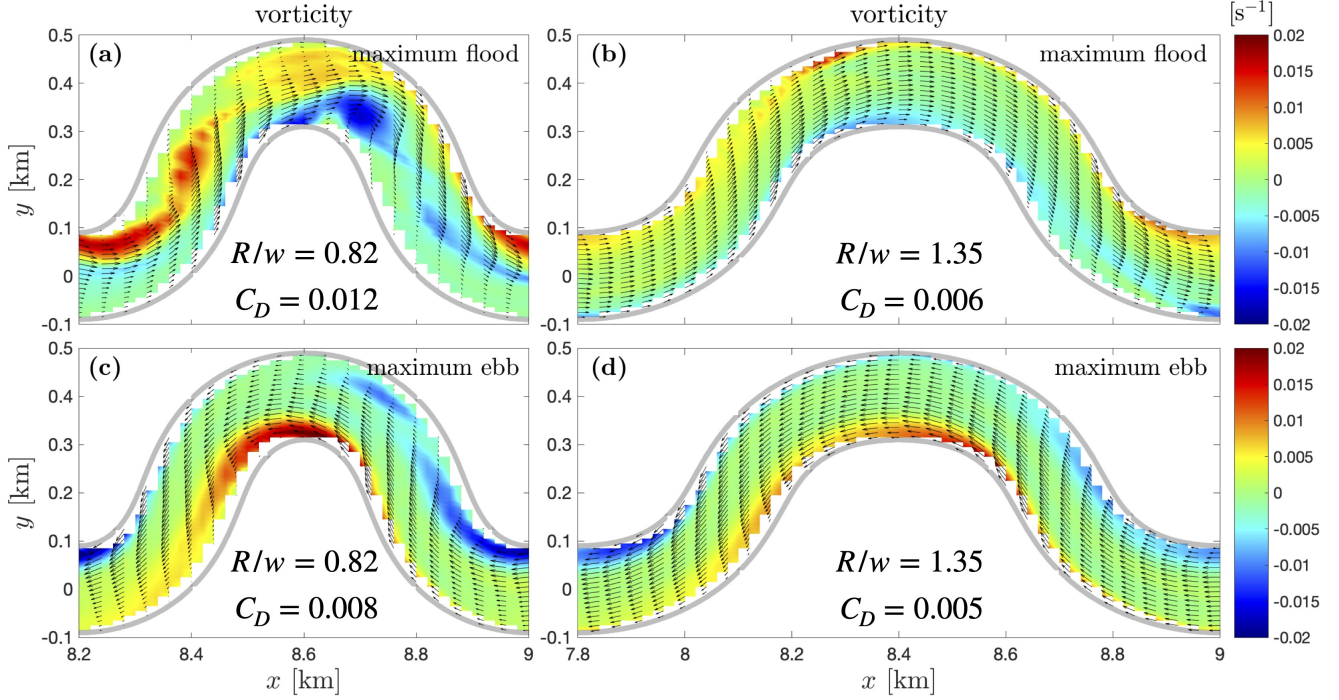


Figure 8: Vorticity field around the channel bend. Panels (a) and (b): maximum flood tide; panels (c) and (d): maximum ebb tide. Panels (a) and (c): a sharp channel bend with  $R/w = 0.82$ ; panels (b) and (d): a smooth channel bend with  $R/w = 1.35$ .  $R$  is the minimum radius of curvature along the channel and  $w$  is the channel width.  $w = 200$  m for both the sharp and smooth bends. The colormap represents the vorticity and arrows show the velocity field. Gray lines mark the river banks. The average drag coefficient in each case is also showed.

The vorticity fields in two channel bends were compared to examine the effects of curvature on flow separation (Figure 8). The two bends have identical channel widths but different minimum radius of curvature and thus different  $R/w$ . In the sharp bend, flow separation is strong, and high vorticity is shed from the inner bank and injected into the main flow (Figure 8 (a) (c)). However, in the smooth bend, flow separation is weak with no change in the main flow width and no recirculating lee eddy is formed. Also, the deflection of the velocity field is minimal, and the high vorticity fluid generated near the wall remains attached (Figure 8 (b) (d)). Not surprisingly, the  $C_D$  in this smooth bend is much less than that of the sharp bend, i.e. an average value of 0.006 compared to 0.01.

Vorticity in the sharp bend is stronger during flood tide than ebb tide, which is consistent with the stronger flow separation (and larger drag) during the deeper flood tide. The more complex vorticity field during flood tide is probably because deeper water makes flow separation less inhibited by bottom friction, and stronger lateral

417 circulation may also contribute to flow complexity (e.g. Kranenburg et al., 2019). In the smooth bend where flow  
418 separation is relatively weak, vorticity is stronger during ebb tide. This is because the current is stronger during  
419 ebb tide due to shallower water and a smaller cross-sectional area, creating greater shear and vorticity.

420 The dependence of flow separation and drag on bend sharpness is not only through the radius of curvature  $R$ ,  
421 but also the width  $w$ . Smaller  $R$  represents sharper bends, while larger  $w$  means sharper curvature of the inner  
422 bank where flow separation happens. Larger  $w$  also leads to larger lateral variation in depth averaged velocity and  
423 stronger adverse pressure gradient near the inner bank that facilitates flow separation. James et al. (2001) showed  
424 that in the cases of wide channels in the laboratory, flow separation occurred and induced considerable energy  
425 dissipation, but no such separation occurred in narrow sinuous channels with same radius of curvature. They also  
426 observed a significant difference in resistance between the narrow and wide channels due to this additional energy  
427 loss associated with flow separation. Our modeling results showed similar results in which flow separation became  
428 weaker as channel width decreased while radius of curvature was kept constant. Detailed comparison of flow  
429 structure is not shown here, but the calculated  $C_D$  from the model results are summarized below in Figure 9.

### 430 **4.3 Drag coefficient diagram**

431 Eight models representing a range of channel geometries (different  $R$ ,  $w$  and  $H$  values) were built to examine the  
432 influence of  $H/w$  and  $R/w$ . Some representative channel shapes are exhibited in Figure A.1. The sinuous channel  
433 shapes are created using a series of sine-generated functions (Langbein and Leopold, 1970) and details are shown  
434 in Appendix A.

435 Drag coefficients calculated in all eight models are summarized in Figure 9 (a). Generally  $C_D$  shows an  
436 increasing trend with  $H/w$  in all the models. Within this dependence on  $H/w$ , smaller values of  $R/w$  are associated  
437 with increased  $C_D$ . The diagram illustrates how across a range of model configurations, larger  $H/w$  and smaller  
438  $R/w$  lead to larger  $C_D$ , as shown in sections 4.1 and 4.2.

439 Analysis of the theoretical flow separation model in section 5 suggests to non-dimensionalize  $H$  using the  
440 along-channel bend length  $L$  instead of  $w$ . The physical explanation of the dependence of  $C_D$  on  $H/L$  will  
441 be discussed in section 5, but for the sake of comparison, the diagram as a function of  $H/L$  is also plotted in  
442 Figure 9 (b). The conclusion is similar in that  $C_D$  increases with  $H/L$  and decreases with  $R/w$ , but using  $H/L$   
443 gives a better collapse of the  $C_D$  data and higher  $R^2$  than using  $H/w$ .

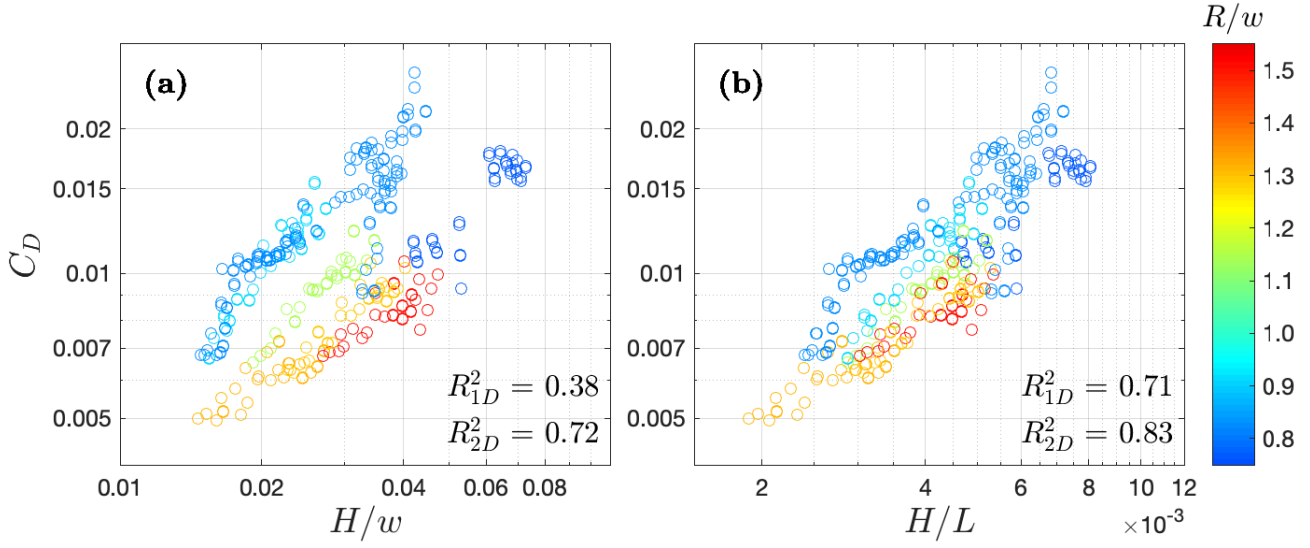


Figure 9: **(a)** The drag coefficient as a function of  $H/w$  with different  $R/w$  values. **(b)** The drag coefficient as a function of  $H/L$  with different  $R/w$  values. Different colors of the data points denote different  $R/w$  values, as is shown on the colorbar.  $R^2_{1D}$  represents the statistical  $R^2$  from linear regression of  $C_D$  on  $H/w$  or  $H/L$ ;  $R^2_{2D}$  represents the statistical  $R^2$  from linear regression of  $C_D$  on both  $H/w$  or  $H/L$  and  $R/w$ .

## 5 Theoretical flow separation model

In this section, we introduce a theoretical model based on boundary layer separation and compare it with numerical results to understand the parameter dependence of  $C_D$ . Outside the boundary layer, flow accelerates as it approaches an island, headland or channel bend, and decelerates after passing by the tip or apex, forming an adverse pressure gradient behind the tip or apex. The adverse pressure gradient is imposed by the outer potential flow onto the viscous boundary layer, which therefore decelerates and even reverses flow near the boundary and leads to boundary layer separation (Signell and Geyer, 1991). In a sinuous channel with limited width, the boundary layer is not always distinguishable from the main flow, but the basic physics are the same as the “outer potential flow and viscous boundary layer” model. Therefore, in this theoretical model, we will first assume potential channel flow to quantify the flow field and then include friction and viscosity to investigate the boundary layer separation.

### 5.1 Potential flow in an idealized sinuous channel

The planform of classical type meanders shows a variation in radius of curvature from a minimum at the bend apexes to infinity at the crossovers between bends (Parsons, 2003). Therefore, in the theoretical model, an idealized flat-bottom channel is built with the centerline radius of curvature described by

$$R = \frac{R_0}{\sin(\pi s/L)}, \quad (8)$$

in which  $s$  is the along-channel distance and  $L$  is the channel bend length.  $R_0$  is the radius of curvature at the bend apex, which is also the smallest radius along the channel. The channel bend is symmetric around the bend apex. We also assume that the radius of curvature increases linearly across the channel (e.g. Leopold, 1960), so that the radius at the inner bank is  $R - w/2$  and the radius at the outer bank is  $R + w/2$ .

The potential flow solution in the idealized channel is derived in Appendix C. The cross-channel velocity profile shows an inversely proportional functional form of  $u = K/r$ , in which  $K$  is a constant and  $r$  is the cross-channel distance (Leopold, 1960). Therefore, the maximum velocity appears near the inner bank, which is consistent with the numerical result in Figure 4 (b1) and (c) as well as other research including Blanckaert (2015) and Kranenburg et al. (2019). The velocity along the inner bank of the channel can be expressed as

$$u_{inner} = \frac{U_0}{\left(\frac{R}{w} - \frac{1}{2}\right) \ln \left(\frac{R+w/2}{R-w/2}\right)}, \quad (9)$$

with  $U_0$  being the uniform incident flow and  $R = R(R_0, s)$ . Flow near the inner bank accelerates as it enters the bend and then decelerates after passing by the bend apex. The maximum inner bank velocity is found at the bend apex.

## 5.2 Adverse pressure gradient around the channel bend

The dominant along-channel momentum balance in the horizontal boundary layer (Signell and Geyer, 1991) is

$$g \frac{\partial \eta}{\partial s} = -u \frac{\partial u}{\partial s} - C_f \frac{u^2}{H}. \quad (10)$$

where  $u$  represent the local along-channel velocity instead of the cross-sectional average  $U$ , and non-inertial effects of curvilinear coordinates are neglected. The unsteady term is negligible because the tidal period is much longer than the timescale of flow passing through one channel bend. The advection term containing  $v$  is also relatively small, and baroclinic effects are ignored because we have assumed homogeneous flow in the theoretical model. Bottom friction is more important than the horizontal viscosity in shallow flows (e.g. Wolanski et al., 1984; Pattiaratchi et al., 1987; Signell and Geyer, 1991), so the horizontal viscous term is also neglected.

In the simplified momentum budget (10), the pressure gradient (the left side term) is balanced by advection (the first term on the right side) and friction (the second term on the right).  $C_f$  is the friction coefficient which describes the drag related to bed skin friction, which is the dominant source of drag in the absence of flow separation.  $C_f$  is set to be 0.004, a value similar to the  $C_D$  of the straight channel numerical model and that predicted by (7) with a

482 bottom roughness of 2 mm and water depth of  $\sim 3 - 4$  m.

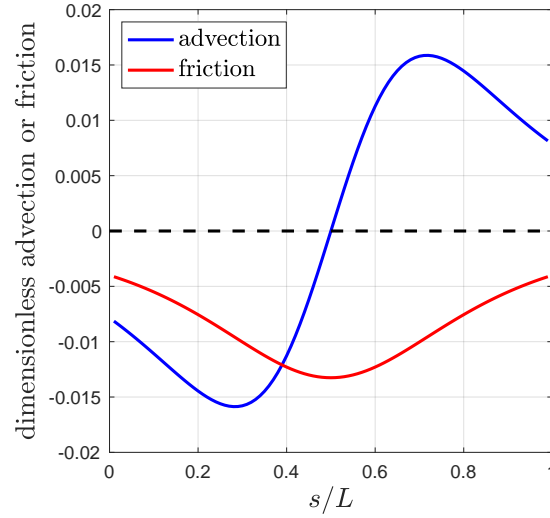


Figure 10: Advection and friction terms in (10) as a function of along-channel distance  $s$  in the theoretical flow separation model.  $L$  is the along-channel bend length.  $s/L = 0.5$  represents the bend apex. Both terms are non-dimensionalized by  $U_0^2/H$ . As representative values, we set  $H/L = 0.005$  and  $R/w = 1$ .

483 The pressure gradient associated with potential flow can be obtained by substituting the potential flow solution  
 484 (9) into (10). We use the inner bank velocity because flow separation happens in the boundary layer near the inner  
 485 bank. These two right-side terms that determine the pressure gradient are plotted in Figure 10. The friction term  
 486 always results in a favoring pressure gradient. The advection term causes a favoring pressure gradient before the  
 487 bend apex where flow is accelerated and sets up an adverse pressure gradient behind the bend apex where flow is  
 488 decelerated. Therefore, flow separation can happen when the advection term exceeds friction and a strong adverse  
 489 pressure gradient occurs behind the bend apex.

### 490 5.3 Parameter dependence of flow separation and drag coefficient

491 Flow separation can be predicted by taking the ratio of the advection term to the friction term. Using the potential  
 492 flow solution, the advection-friction ratio  $K_r$  can be expressed as

$$K_r = -u \frac{\partial u}{\partial s} / C_f \frac{u^2}{H} = \alpha \beta \frac{H}{C_f L}, \quad (11a)$$

$$\alpha = \frac{1}{R - w/2} \left( 1 - \frac{1}{\left(\frac{R}{w} + \frac{1}{2}\right) \ln \left(\frac{R+w/2}{R-w/2}\right)} \right), \quad (11b)$$

$$\beta = -\pi R \cot \left( \frac{\pi s}{L} \right). \quad (11c)$$



493  $\alpha$  is related to potential flow with curvature, i.e.  $\partial u/\partial R$ ;  $\beta$  is associated with the sinuous channel shape, i.e.  $\partial R/\partial s$ .  
 494 For this analysis,  $s/L$  is chosen as 0.75 where advection (or adverse pressure gradient) reaches its maximum  
 495 (Figure 10). Since both  $\alpha$  and  $\beta$  are only functions of  $R_0/w$ , the advection-friction ratio can be re-written as

$$K_r = \frac{H}{C_f L} \mathcal{F} \left( \frac{R}{w} \right). \quad (12)$$

496 Henceforth we drop the subscript of  $R_0$  for convenience and  $R$  will represent the smallest centerline radius of  
 497 curvature along the channel bend. The ratio  $K_r$  depends on two dimensionless number,  $H/(C_f L)$  and  $R/w$ . This  
 498 dependence on dimensionless water depth and curvature ratio is in agreement with the parameter dependence of  $C_D$   
 499 in the numerical results in section 4. The water depth  $H$  can be either scaled by channel width  $w$  or along-channel  
 500 length  $L$ , and both make sense physically. The dependence on  $H/w$  lies in the fact that the width of separation  
 501 zone scales with water depth so the fraction of the main flow impacted by flow separation depends on  $H/w$ .  $H/L$   
 502 comes from by taking the ratio of advection to friction that predicts when flow separation happens.  $C_f$  is the  
 503 bottom friction coefficient, which is a constant in the theoretical model and only varies within a small range in the  
 504 numerical models, so the effect of  $C_f$  is not addressed in detail.  $H/(C_f L)$  is analogous to a Reynold's number  
 505 based on friction instead of viscosity (Pingree and Maddock, 1980; Signell and Geyer, 1991). Blanckaert and  
 506 De Vriend (2010) and Blanckaert (2011) reported two similar control parameters of sinuous dynamics  $C_f^{-1} H/w$   
 507 and  $w/R$ , although that analysis was based on a different conceptual model and focused on the magnitude of  
 508 secondary flow.

509 The theoretical ratio  $K_r$  is plotted as a function of  $H/L$  and  $R/w$  in Figure 11 **(a)**.  $K_r$  increases with  $H/L$   
 510 and decreases with  $R/w$ , suggesting that flow separation is stronger when  $H/L$  is larger and  $R/w$  is smaller. This  
 511 is consistent with the similar dependence of  $C_D$  on  $H/L$  and  $R/w$  in section 4, because  $C_D$  increases with greater  
 512 form drag due to flow separation in the sharp bend models.

513  $K_r = 1$  is marked by a black line in Figure 11 **(a)**. For  $K_r > 1$ , advection dominates friction and flow sep-  
 514 aration is relatively strong, while for  $K_r < 1$ , friction dominates advection and flow separation is weak. This  
 515 theoretical prediction is consistent with our numerical model results. For example, the simulation shown in Fig-  
 516 ure 8 **(b)** and **(d)**, with an  $H/L \sim 0.002 - 0.003$  and  $R/w = 1.35$ , yields  $K_r < 1$  in the theoretical model and  
 517 exhibits weak flow separation in the simulation. Most of the other simulations fall in the regime of  $K_r > 1$  and  
 518 have relatively strong flow separation and larger  $C_D$ .

519 Leeder and Bridges (1975) proposed a dimensionless graph to predict flow separation as a function of bend  
 520 sharpness  $R/w$  and Froude number  $F_r$ . Our research focuses on relatively low  $F_r$  flow between 0.1 – 0.2, and we

observed flow separation for an  $R/w$  of around 0.7 – 1.3, which is consistent with that study. James et al. (2001) found that the curvature ratio was 2.3 for a narrow sinuous channel without flow separation and 0.89 and 0.54 for two wide sinuous channels with flow separation, with  $H/L$  of approximately 0.007, although this parameter is not directly reported. Their narrow sinuous channel falls above the  $K_r = 1$  line on our diagram (Figure 11 (a)) and the wide sinuous channels are below the line, consistent with the theoretical model. From field observations, flow separations at a sharp bend on the River Dean, with  $H/L = 0.04$  and  $R/w = 1.4$  (Ferguson et al., 2003), and on the Tollense River at a bend with  $H/L = 0.015$  and  $R/w = 1.0$  (Schnauder and Sukhodolov, 2012) were also consistent with the prediction given by Figure 11 (a). These two rivers were both relatively deeper than our models. In rivers, the existence of a point bar decreases water depth near the inner bend and may inhibit flow separation such that rivers must be deeper than tidal channels with similar bend sharpness for flow separation to happen.

While the influences of  $H/L$  and  $R/w$  are investigated in this research, the bottom friction coefficient  $C_f$  also appears in the theoretical result (12). The bottom roughness is uniform in all the numerical models, so there is not sufficient parameter range to investigate the influence of  $C_f$  on flow separation.  $C_f$  depends on water depth, but the influence of water depth is greater on  $H/L$  than  $C_f$ . James et al. (2001) reported that vegetation can inhibit flow separation in channel bends and decrease the drag. Their research supports our theoretical result that increasing  $C_f$  will decrease the advection-friction ratio  $K_r$  and suppress flow separation, although in James et al. (2001)  $C_f$  is increased by vegetation stem friction rather than bottom roughness.

Comparing Figure 9 (b) to Figure 11 (a), we can observe similar dependencies of  $K_r$  and  $C_D$  on  $H/L$  and  $r/w$ . This correspondence between the theoretical model and numerical simulations provides further support that the increased drag coefficient is due to flow separation, and leads to the possibility of predicting  $C_D$  using the theoretical flow separation model. The ratio  $K_r$  can serve as a correction coefficient or amplification factor to the drag coefficient, i.e.  $C_D = \mathcal{G}(K_r)C_f$ . We choose a simple linear expression,

$$C_D = (K_r + 1)C_f. \quad (13)$$

Although secondary circulation can be another essential factor in increasing drag, this is not included in (13) as the effect of flow separation is dominant in the sharp channel bends of our models. This linear expression does not account for the effect of  $C_f$  on flow separation drag either, because it cancels with the  $C_f$  in the denominator of  $K_r$ . These results assume a fixed value for  $C_f$ , but this linear expression, as a speculation, can be used to represent the effects of the two geometric parameters  $H/L$  and  $R/w$  on  $C_D$ .

The predicted  $C_D$  given by (13) is plotted as the dashed line in Figure 7, which agrees reasonably well with

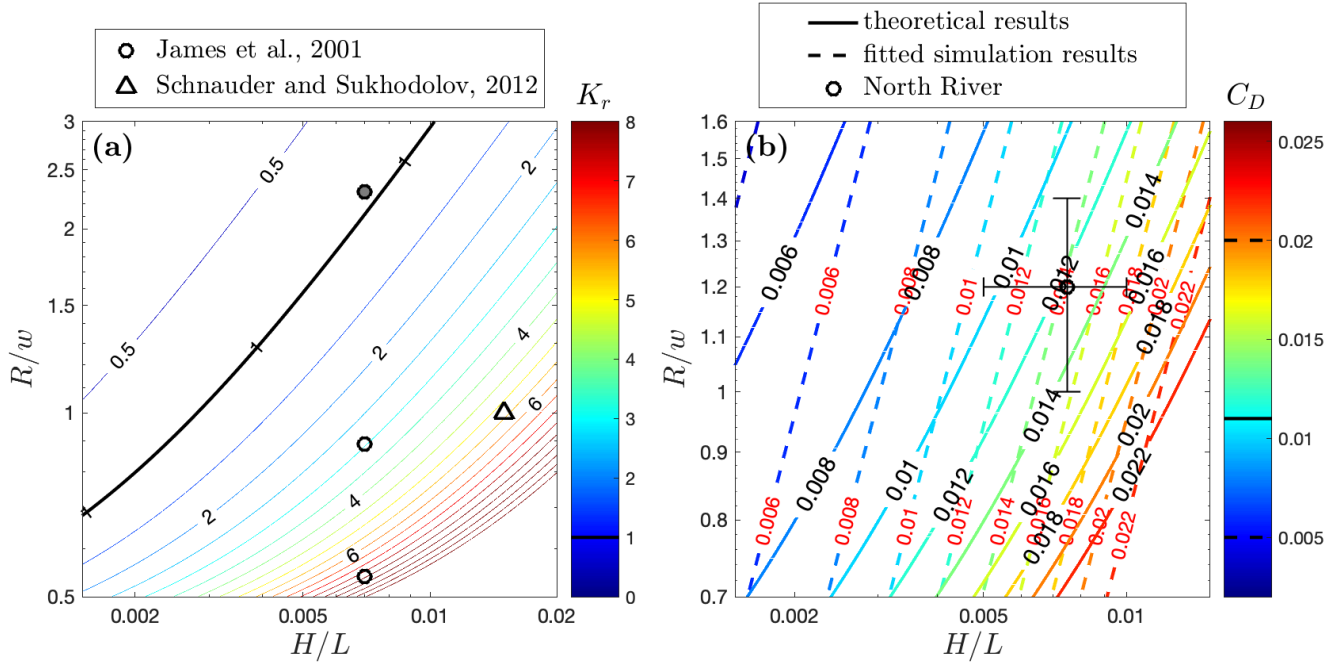


Figure 11: **(a)**: Contours of the ratio of advection to friction  $K_r$  as a function of  $H/L$  and  $R/w$ .  $K_r = 1$  is marked by the black lines on the colorbar and contours. Circles represent laboratory experiments by James et al. (2001). The hollow circles show cases where flow separation happens; the circle filled with gray color shows the case where flow separation does not happen. The triangle represents observations by Schnauder and Sukhodolov (2012) at one bend on the Tollense River where flow separation happens. **(b)**: Contours of the drag coefficient  $C_D$ . Solid lines represent the  $C_D$  predicted by (13) using  $K_r$  of the theoretical model. Dashed lines represent the 2D linear fit of numerical results showed in Figure 9 (b). The circle shows the estimation of geometric parameters for the North River, with error bars representing spatial and temporal variability. The solid black line on the colorbar represents the average  $C_D$  on the North River and two dashed black lines represent the range of observed  $C_D$  on the North River.

our numerical results. The parameter  $H/L$  is converted to  $H/w$  for the convenience of comparison. A 2D linear fit is applied to the numerical results (Figure 9 (b)) and is compared with the theoretical prediction by (13). The theoretical prediction shows consistency with the numerical results in the increasing trend with  $H/L$  and decreasing trend with  $R/w$  as well as the magnitude of  $C_D$ , even though we are only using a linear relationship (13) with constant  $C_f$ . For the North River estuary that initially motivated this study, the two geometric parameters are estimated from Kranenburg et al. (2019), with average  $H/L \approx 0.008$  and  $R/w \approx 1.2$ . Using these values, the effective drag in the North River predicted by Figure 11 (b) is around  $0.012 \pm 0.003$ , whereas observations found an average  $C_D$  of  $\sim 0.011$ , ranging between 0.005 and 0.02 (Kranenburg et al., 2017). It is also worthwhile to note that the parameter dependence discussed above is only correct in the regime where flow separation happens. When there is no flow separation, e.g. when water is very shallow or the bend is very smooth,  $C_D$  will either decrease with  $H$  as is predicted by (7) for straight channels, or show a different parameter dependence if the increased drag is predominately due to secondary circulation.

## 561 **6 Discussion**

### 562 **6.1 Flow separation and drag increase in sinuous channels**

563 This research shows that the drag coefficient can be increased by channel meanders as a result of flow separation.  
564 Therefore, we suggest modifications to traditional drag coefficients for flow in sinuous tidal channels, e.g. an  
565 increase of up to a factor of 2 – 7 depending on the strength of flow separation. Such a significant increase to  
566 the drag can increase water level slope and result in considerable water level changes along the channel, which  
567 influences wetland inundation and regulates the distribution of vegetation. The increased drag in sinuous channels  
568 can also affect tidal propagation (larger amplitude decay and increased phase lag) and potentially storm surge  
569 flooding. A sinuous planform may also enhance nonlinear tidal transformation and affect the growth of overtides,  
570 which then affects sediment transport.

571 Apart from the effects of increased drag, flow separation due to channel curvature has the potential to enhance  
572 erosion near the inner bank at bend apex, because it increases local velocity and injects fluid from the inner bank  
573 to the main flow. Erosion associated with flow separation could alter the sinuous channel morphology, e.g. by the  
574 erosion of a point bar. Reversal in the lateral circulation associated with the baroclinic pressure gradient has also  
575 been suggested as enhancing erosion near the inner bank and inhibiting formation of a point bar (Kranenburg et al.,  
576 2019). Flow separation together with the reversed lateral circulation can explain the absence of a point bar in many  
577 sharp bends in tidal meanders, while the absence of a point bar in turn allows for flow separation and the reversed  
578 lateral circulation. Flow separation increases deposition in the recirculating dead zone beyond the bend apex where  
579 current is very weak, e.g. Schmidt (1990) found that sandbars form beneath recirculation zones in the Colorado  
580 River in the Grand Canyon. As a result, sandbars can grow in the lee of bends where flow separation occurs,  
581 and this growth may act differently in unidirectional flow of rivers than the bidirectional flow of tidal channels.  
582 The dead zone created by flow separation could also affect along-channel scalar transport by trapping tracers and  
583 increasing longitudinal mixing and dispersion (Thackston and Schnelle, 1970).

584 Key parameters that influence the increased drag coefficient were discussed in this paper —  $H/L$  (or  $H/w$ )  
585 and  $R/w$  — but other factors may also affect flow separation drag. Signell and Geyer (1991) mentioned that  
586 local acceleration can cause an adverse pressure gradient over headland scales comparable to the tidal excursion  
587 (5 – 10 km), which therefore impacts the strength of flow separation and magnitude of drag. In the sinuous  
588 channels used in this study, the channel bends are around 100 – 1000 m in length, which is much smaller than  
589 the tidal excursion so the effect of tidal flow unsteadiness can be neglected. However, large channel bends with  
590 lengths of up to 10 km are also observed in nature (e.g. Marani et al., 2002) and the unsteadiness associated

with tidal currents need to be considered in these cases. In addition, interactions between channel bends and the accumulation of instability through multiple bends may affect the strength of flow separation. The vortices shed from an upstream bend due to flow separation can interact with the vorticity field of the downstream bends, which then impacts flow separation and the drag, and the cumulative effect remains as an open question.

This research focused on the increased drag coefficient in sinuous channels associated with flow separation. Secondary circulation, which can enhance the bottom velocity and bottom stress, is another mechanism through which the sinuous planform can increase drag (e.g. Chang, 1984; Pein et al., 2018). We also observed increased bottom friction associated with secondary circulation in the modeling results. The drag coefficient increase due to secondary circulation is generally less than 30%, which is negligible compared to the total drag increase associated with flow separation in these very sharp channel bends (a factor of 2 – 7). However, in the channel bends that were less sharp, flow separation was weaker and secondary circulation could be a bigger factor in increasing drag. Blanckaert and De Vriend (2010) and Blanckaert (2011) quantitatively expressed the magnitude of secondary circulation as a function of  $C_f^{-1}H/w$  and  $w/R$ , and this provides valuable reference for exploring the parameter dependence of the  $C_D$  associated with secondary circulation.

In the numerical study,  $C_D$  is calculated based on  $U$ , the channel average velocity, as the velocity field shows large lateral variations in sinuous models. However, in field observations the channel average velocity is hard to directly measure, and  $C_D$  is usually applied to velocity measurements at one location. If field observations are made in the center of the channel where the main flow is accelerated as a result of flow separation,  $U$  in the denominator of (3) will be overestimated and the measured  $C_D$  will become smaller than that predicted by this study. On the contrary, if the current meter is located close to the dead zone, the measured  $C_D$  will become larger instead.

## 6.2 Similarity and differences between rivers and tidal channels

River meanders and tidal meanders show strong similarity in their planform geometry (Marani et al., 2002). The degree of meandering of a channel is usually quantified by the channel sinuosity  $L/L_x$  (the ratio between along-channel distance and Cartesian channel length or meander wavelength) and  $L_x/w$  (the ratio between meander wavelength and channel width). Previous studies have found that fluvial and tidal meanders have similar  $L/L_x$  and  $L_x/w$  values, across widths and wavelengths over three to four orders of magnitude (Leopold and Wolman, 1960; Leopold et al., 2012; Marani et al., 2002). The similarity exhibited by river and tidal meanders also lies in the bend sharpness, which is customarily quantified as  $R/w$ . Two thirds of the  $R/w$  values lie between 1.5 and 4.3 in a sample of 50 rivers (Leopold and Wolman, 1960), and  $R/w$  is found to be 1.6 – 5 in tidal meanders (Marani et al., 2002). Very sharp bends in river meanders can have an  $R/w$  as small as 1.0 (Schnauder and Sukhodolov,

621 2012) and 0.6 (Nanson, 2010), and in tidal meanders the smallest  $R/w$  can reach 0.5 near some sharp bend apexes  
622 (Marani et al., 2002).

623 The morphological difference between river meanders and tidal meanders lies in their aspect ratio (channel  
624 width to depth,  $w/H$ ), and typically, the cross-channel depth distribution. In river channel bends, the aspect ratio  
625 usually falls between 10 and 50 (Millar, 2000). Tidal flat channels tend to have aspect ratios similar to rivers, in the  
626 range of 8 – 50 (Marani et al., 2002), but in salt marsh channels the aspect ratio is typically around 6 (Marani et al.,  
627 2002), making them narrower or deeper than river meanders. In addition, vegetation along the salt marsh channels  
628 can stabilize banks, reducing channel migration and steepening banks (Redfield, 1972; Gabet, 1998). The cross-  
629 channel depth profile of tidal channels may also differ from rivers, where point bars are commonly found at the  
630 inside of bends (Leopold and Wolman, 1960) due to the cross-channel circulation and sediment transport that leads  
631 to shallower bathymetry at the inside of bends and deeper at the outside. While point bars also can occur in tidal  
632 channels (Barwis, 1977; Fagherazzi et al., 2004), in some sharp tidal channel bends the cross-channel bathymetry  
633 is relatively uniform, with an absence of a distinct point bar (e.g. Barwis, 1977; Nidzieko et al., 2009; Kranenburg  
634 et al., 2019).

635 The study site of the North River does not have distinct point bars, and the numerical models have symmetric  
636 lateral depth structure. A point bar can enhance the friction near the inner bank, i.e increase the  $C_f$  and decrease  
637  $H$  in (12), and thus inhibit flow separation and decrease the form drag. Marriott (1998) found in the laboratory  
638 that when the flow went overbank and became very shallow near the inner bend, flow reversal and separation  
639 were no longer observed, which is consistent with our results. The prevalence of point bars may explain why  
640 flow separation and the associated drag increase are less common in the river literature. Therefore, the effect of  
641 cross-channel bathymetry profile needs to be carefully examined in the prediction of flow separation and drag  
642 coefficient. On the other hand, flow separation is reported in some rivers that are relatively deeper than our models  
643 (e.g. Ferguson et al., 2003; Schnauder and Sukhodolov, 2012), so this form drag may still be expected to occur in  
644 relatively deep rivers or tidal channels with a point bar.

645 Rivers and tidal channels also differ markedly in their hydrodynamic forcing. Rivers are only controlled by  
646 unidirectional fluvial discharge, while tidal channels are influenced by bidirectional tidal flow. Estuarine tidal  
647 channels also have inputs of freshwater that create density differences and influence the dynamics. Baroclinic  
648 pressure gradients and stratification contribute to the flow structure in many tidal channels, including by modifying  
649 turbulence (Geyer, 1993) and lateral circulation (Chant and Wilson, 1997; Nidzieko et al., 2009). The differences  
650 in forcing correspond with differences in time scales of variability between rivers and tidal channels. Bidirectional  
651 tidal flow changes regularly at semi-diurnal to spring-neap periods, while in rivers, major discharge events may

652 occur once a year or less frequently.

653 The theoretical model is based on the assumption that fluid is homogeneous. In our numerical models, the  
654 estuary was weakly stratified during early flood tide and early ebb tide and was vertically well-mixed during other  
655 tidal stages. Differences in lateral circulation were also observed between flood and ebb tides, associated with  
656 lateral baroclinic pressure gradients. Although the effects of stratification and lateral circulation on  $C_D$  still require  
657 further investigation, the theoretical model without these factors can account for most of the variability in  $C_D$ ,  
658 suggesting that stratification and baroclinic pressure gradients are secondary factors in weakly stratified channels.  
659 Conclusions of this study are not only restricted to estuarine tidal channels with mixed fresh and salt water but can  
660 also be applied to tidal freshwater or fluvial rivers with similar planform and cross-sectional geometry.

## 661 7 Conclusion

662 The increased drag coefficient is observed in sinuous channel models, consistent with observations from the North  
663 River estuary. This drag increase leads to faster tidal amplitude decay and larger tidal phase lag in estuarine  
664 channels with curvature. The increased drag coefficient is mainly due to flow separation, which creates a low  
665 pressure zone in the lee of bends and produces form drag. The curved estuarine channel also has larger energy  
666 dissipation as a result of decreased effective channel width, increased velocity in the center of the channel, and  
667 weakened stratification. The increased drag coefficient in sinuous channels depends on two geometric parameters,  
668 i.e. it increases with  $H/L$ , where  $H$  is the water depth and  $L$  is the along-channel bend length, and decreases with  
669  $R/w$ , where  $R$  is the bend radius of curvature and  $w$  is channel width. A theoretical boundary layer separation  
670 model successfully represents this parameter dependence, which is based on the relative dominance of advection  
671 and friction. The theoretical model suggests that flow separation shows similar dependence on  $H/L$  and  $R/w$  and  
672 predicts conditions for flow separation to happen:  $R/w < 1$  for “shallow” channels, e.g.  $H/L \sim 0.003$  or an  
673 aspect ratio of  $\sim 40$ ;  $R/w < 1.5$  for “intermediate” channels, e.g.  $H/L \sim 0.006$  or an aspect ratio of  $\sim 20$ ;  
674  $R/w < 2$  for “deep” channels, e.g.  $H/L \sim 0.01$  or an aspect ratio of  $\sim 10$ . As a result, the drag coefficient can  
675 be increased by a factor of 2 – 7 depending on channel geometry and strength of flow separation. A point bar  
676 can decrease water depth near the inner bank and potentially inhibit flow separation and prevent the drag increase.  
677 Although we focused on estuarine channels without a point bar, this research still suggests that the increased drag  
678 coefficient associated with flow separation is expected in river or tidal meanders with a point bar, when the channel  
679 is narrow or deep enough.

## 680 **A Sinuous channel shape**

681 The mathematical expressions for setting sinuous channel shapes are proposed by Langbein and Leopold (1970)  
 682 based on the theory of minimum variance. The direction angles of channel centerline are set as

$$\theta = A \sin(s), \quad (14)$$

683 in which  $A$  determines the maximum angle of deviation from the mean downstream direction. The Cartesian ex-  
 684 pression of channel centerline is generated in an integral form with respect to the angle and along-channel distance,

$$x = X \int \cos \theta ds; \quad y = Y \int \sin \theta ds. \quad (15)$$

685  $X, Y$  determine the Cartesian length ( $L_x$ ) and Cartesian width ( $L_y$ ) of the channel bend, respectively. Four repre-  
 686 sentative channel shapes are exhibited in Figure A.1.

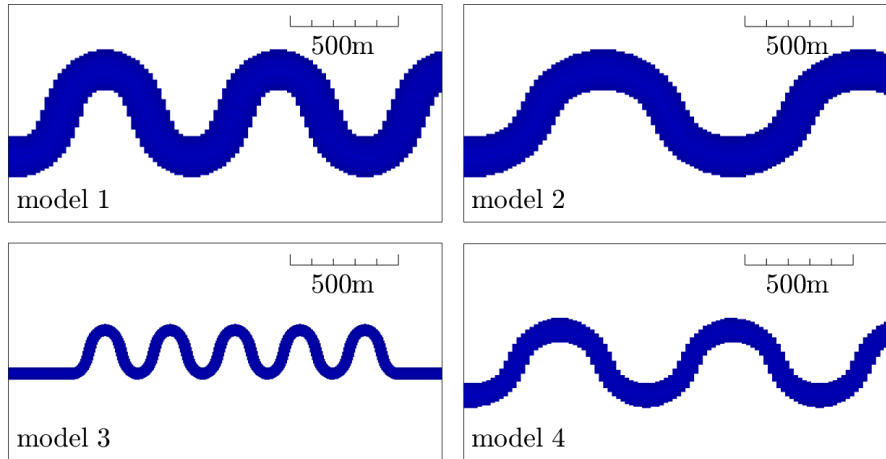


Figure A.1: Different channel shapes used in the models. The scale is as marked in the plot.

## 688 **B Integral form of the momentum budget**

689 Simplify (4) and the integral form of the momentum equation for the straight channel can be written as

$$\int_{A_{CS1}} p dS - \int_{A_{CS2}} p dS + \int_{A_b} p \xi_x dS + \int_{A_b} \tau_{bx} dS = 0. \quad (16)$$

690 where  $A_{CS1}$  and  $A_{CS2}$  represent the cross-sectional areas at each end of the control volume and  $A_b$  represents the  
 691 area of the channel bed.  $\xi_x$  corresponds to the projection in  $x$ -direction. There is no integrated pressure on the



692 sidewalls because the projected area in the  $x$ -direction is zero in the straight model so the integral over  $A_w$  has  
 693 been removed from (4). The unsteady and advection terms are neglected, and only barotropic pressure is included  
 694 because baroclinic effects are small.

695 Momentum balance is achieved among the total pressure difference force

$$P_{diff,total} = \int_{A_{CS1}} p dS - \int_{A_{CS2}} p dS, \quad (17)$$

696 the pressure force exerted by the decreasing thalweg depth along the channel (the bottom-slope effect)

$$P_{slope} = \int_{A_b} p \xi_x dS = \int_{A_b} \rho g (h + \eta) \xi_x dS, \quad (18)$$

697 and the bottom friction  $F_{bot}$  (the last term in (16)). A considerable part of  $P_{diff,total}$  is contributed by the channel  
 698 depth difference between  $CS1$  and  $CS2$  and this part is exactly canceled by the bottom-slope pressure force  $P_{slope}$   
 699 in the momentum budget. To quantify the pressure difference created only by the water level and get rid of the  
 700 bottom-slope effect, we write a pressure correction term by applying linear approximation to the water level field  
 701 in (18) (i.e. the water level linearly changes along the channel)

$$P_{corr} = \int_0^w \frac{1}{2} (h_1 + \eta_1 + h_2 + \eta_2) (h_1 - h_2) dy. \quad (19)$$

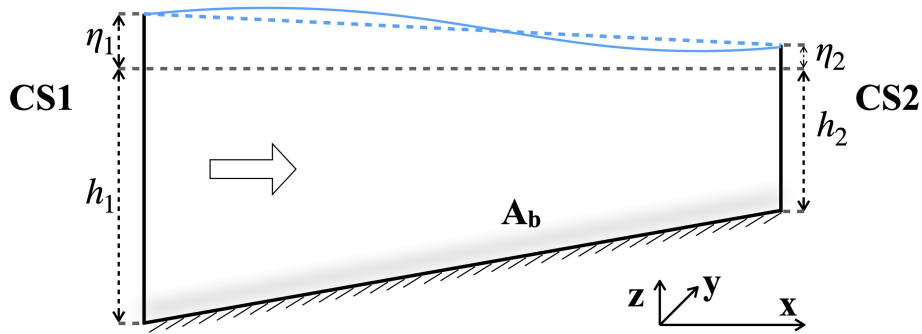


Figure B.1: Schematic of the sideview of the straight channel with decreasing thalweg depth.  $CS1$  and  $CS2$  represent the cross-sections at each end of the control volume and  $A_b$  represent the channel bed.  $h_1$  and  $h_2$  represent the depth of channel bed below mean water level;  $\eta_1$  and  $\eta_2$  represent the water level.  $h_1, h_2, \eta_1$  and  $\eta_2$  are functions of  $y$ . The solid blue line is the water level and the dashed blue line is the linear approximation of the water level.

702 The bottom-slope pressure force  $P_{slope}$  in (18) is calculated directly by integrating over the bottom  $A_w$ . The  
 703 pressure correction term  $P_{corr}$  in (19) is calculated based on the linear approximation by using only water level and  
 704 channel depth at the ends of the control volume.  $P_{corr}$  can balance  $P_{slope}$  (Figure B.2) and the remaining “form

705 drag” in the straight channel is zero, by subtraction (19) from (18). Therefore, we can write the corrected pressure  
 706 difference force by subtracting  $P_{corr}$  from (17)

$$P_{diff} = \int_{A_{CS1}} p dS - \int_{A_{CS2}} p dS - P_{corr}, \quad (20)$$

707 which only accounts for the pressure difference associated with water level and does not incorporate the bottom-  
 708 slope effect. In the straight channel, the corrected pressure difference  $P_{diff}$  is generally equal to the bottom friction  
 709  $F_{bot}$  for both flood and ebb tide (Figure B.2), indicating that the momentum budget closes with these two terms,  
 710 and corresponds to a drag coefficient of 0.003 – 0.004, consistent with the calculation in section 3.1. Therefore,  
 711 the pressure correction based on the linear approximation is effective for removing the bottom-slope effect in the  
 712 straight channel, and this same approach can be applied to the sinuous channel. The pressure force associated with  
 713 bottom slope is much larger than the pressure difference created by water level and the bottom friction (Figure B.2),  
 714 as the bottom slope is greater than the water level slope, which again illustrates the need to remove the bottom-slope  
 715 effect in calculating the momentum budget.

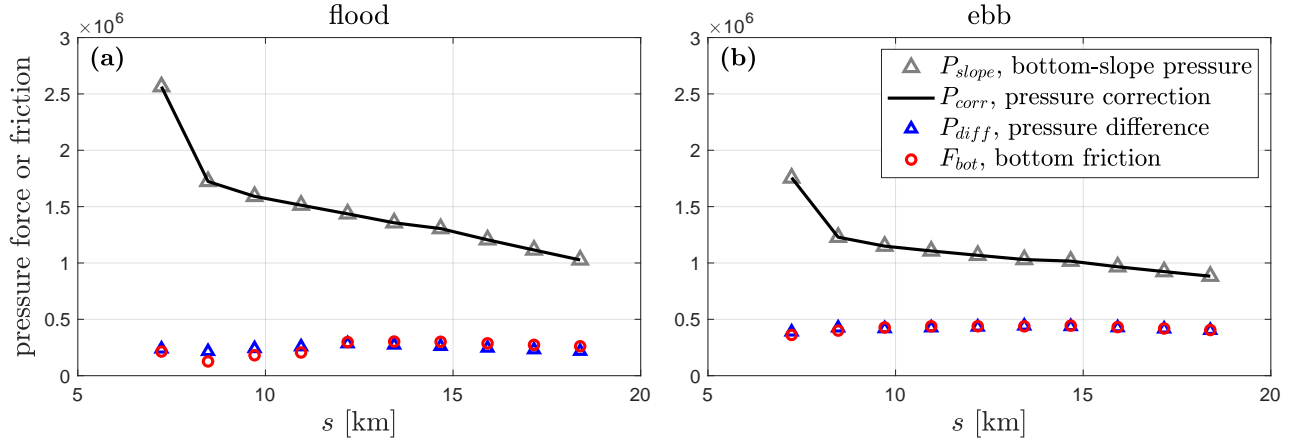


Figure B.2: Pressure force and bottom friction in the momentum budget (16) of the straight channel. **(a)** Maximum flood tide. **(b)** Maximum ebb tide. Blue triangles represent the corrected pressure difference in (20) and red circles represent the bottom friction. Gray triangles are the pressure force associated with along-channel depth decrease calculated directly by integrating over the bottom using (18). Black lines are the pressure correction term used to cancel the bottom-slope effect calculated by using (19).

716 The pressure difference in the sinuous channel is calculated in a similar way as (20) to remove the pressure  
 717 force associated with along-channel depth decrease. The form drag of the sinuous channel is also calculated by  
 718 subtracting the pressure correction term  $P_{corr}$  from the third right-side term in (4),

$$P_{form} = \int_{A_w + A_b} p \xi_x dS - P_{corr}, \quad (21)$$

719 to remove the bottom-slope effect and only keep the form drag associated with water level variations around the  
 720 bend.  $A_w$  is included in (21) for the sinuous channel, which did not appear in the straight channel where there is  
 721 no wall normal to the  $x$ -direction.

## 722 **C Potential flow model**

723 Assume potential flow in a flat-bottom channel and the radius of curvature of the centerline is

$$R = \frac{R_0}{\sin(\pi s/L)}, \quad (22)$$

724 in which  $s$  is the along-channel distance and  $L$  is the channel bend length.  $R_0$  is the radius of curvature at the bend  
 725 apex, which is also the smallest radius along the channel. The channel bend is symmetric around the bend apex.  
 726 We also assumed that the radius of curvature increases linearly across the channel (e.g. Leopold, 1960), so that the  
 727 radius at the inner bank is  $R - w/2$  and the radius at the outer bank is  $R + w/2$ , where  $w$  is the channel width.

728 Assume the flow entering the bend is uniform with velocity  $U_0$  and water depth  $H$ . The along-channel Bernoulli  
 729 equation is

$$gH(s, r) + \frac{1}{2}u(s, r)^2 = gH_0 + \frac{1}{2}U_0^2, \quad (23)$$

730 where both water depth  $H$  and velocity  $u$  are a function of along-channel distance  $s$  and cross-channel distance  
 731  $r$ . We assume no lateral or vertical velocity so  $u$  only represents streamwise velocity. Differentiating (23) in the  
 732 cross-channel direction gives

$$g \frac{\partial H}{\partial r} = g \frac{\partial(H_0 + \eta)}{\partial r} = g \frac{\partial \eta}{\partial r} = -u \frac{\partial u}{\partial r}, \quad (24)$$

733 with  $\eta$  being surface elevation. The cross-channel Euler equation is

$$g \frac{\partial \eta}{\partial r} = \frac{u^2}{r}. \quad (25)$$

734 Substituting (24) into (25) and we obtain

$$u = \frac{K}{r}. \quad (26)$$

735 The cross-channel velocity profile is inversely proportional to cross-channel distance with  $K$  being a constant at  
 736 each cross-section (Leopold, 1960).

$$\int_{R-w/2}^{R+w/2} u(s, r) H(s, r) dr = U_0 H_0 w \quad (27)$$

and the along-channel Bernoulli equation (23), we get an expression to solve for  $K$  (Shapiro and Sonin, 2018),

$$U_0 H_0 w = K H_0 \left( 1 + \frac{U_0^2}{2gH_0} \right) \ln \frac{R + w/2}{R - w/2} - \frac{K^3}{4g(R - w/2)^2} \left( 1 - \left( \frac{R - w/2}{R + w/2} \right)^2 \right). \quad (28)$$

The water level differences are negligible compared to the total water depth in the mass flux (but the water level change related to Bernoulli should never be neglected), so  $K$  can be approximated as

$$K \approx \frac{U_0 w}{\ln \left( \frac{R+w/2}{R-w/2} \right)}. \quad (29)$$

Therefore, we get the inner bank velocity at  $r = R - w/2$ ,

$$u_{inner} = \frac{U_0}{\left( \frac{R}{w} - \frac{1}{2} \right) \ln \left( \frac{R+w/2}{R-w/2} \right)}, \quad (30)$$

with  $R = R(R_0, s)$ .

**Acknowledgements** The authors thank W. R. Geyer for helpful suggestions. T. Bo was supported by the Michael J. Kowalski Fellowship in Ocean Science and Engineering in the MIT-WHOI Joint Program. Support for DKR and the research leading to these results was funded by NSF award OCE-1634480. Model data generated in this study are available at <https://doi.org/10.5281/zenodo.3711648>.

## References

- Apmann, R. P. (1964). A case history in theory and experiment: fluid flow in bends. *Isis*, 55(4):427–434.
- Arcement, G. J. and Schneider, V. R. (1989). Guide for selecting manning’s roughness coefficients for natural channels and flood plains.
- Aubrey, D. and Speer, P. (1985). A study of non-linear tidal propagation in shallow inlet/estuarine systems part i: Observations. *Estuarine, Coastal and Shelf Science*, 21(2):185–205.
- Bagnold, R. A. (1960). *Some aspects of the shape of river meanders*. US Government Printing Office.

754 Barwis, J. H. (1977). Sedimentology of some south carolina tidal-creek point bars, and a comparison with their  
755 fluvial counterparts. *Fluvial Sedimentology*.

756 Blanckaert, K. (2011). Hydrodynamic processes in sharp meander bends and their morphological implications.  
757 *Journal of Geophysical Research*, 116(F1).

758 Blanckaert, K. (2015). Flow separation at convex banks in open channels. *Journal Of Fluid Mechanics*, 779:432–  
759 467.

760 Blanckaert, K. and De Vriend, H. (2010). Meander dynamics: A nonlinear model without curvature restrictions  
761 for flow in open-channel bends. *Journal of Geophysical Research: Earth Surface*, 115(F4).

762 Blanckaert, K., Kleinhans, M. G., McLelland, S. J., Uijttewaal, W. S., Murphy, B. J., van de Kruijs, A., Parsons,  
763 D. R., and Chen, Q. (2013). Flow separation at the inner (convex) and outer (concave) banks of constant-width  
764 and widening open-channel bends. *Earth Surface Processes and Landforms*, 38(7):696–716.

765 Chang, H. H. (1984). Variation of flow resistance through curved channels. *Journal of Hydraulic Engineering*,  
766 110(12):1772–1782.

767 Chant, R. J. and Wilson, R. E. (1997). Secondary circulation in a highly stratified estuary. *Journal of Geophysical*  
768 *Research: Oceans*, 102(C10):23207–23215.

769 Chow, V. T. (1959). Open-channel hydraulics. In *Open-channel hydraulics*. McGraw-Hill.

770 Fagherazzi, S., Gabet, E. J., and Furbish, D. J. (2004). The effect of bidirectional flow on tidal channel plan-  
771 forms. *Earth Surface Processes and Landforms: The Journal of the British Geomorphological Research Group*,  
772 29(3):295–309.

773 Ferguson, R. I., Parsons, D. R., Lane, S. N., and Hardy, R. J. (2003). Flow in meander bends with recirculation at  
774 the inner bank. *Water Resources Research*, 39(11):299–13.

775 Frothingham, K. M. and Rhoads, B. L. (2003). Three-dimensional flow structure and channel change in an asym-  
776 metrical compound meander loop, embarras river, illinois. *Earth Surface Processes and Landforms: The Journal*  
777 *of the British Geomorphological Research Group*, 28(6):625–644.

778 Gabet, E. J. (1998). Lateral migration and bank erosion in a saltmarsh tidal channel in san francisco bay, california.  
779 *Estuaries*, 21(4):745–753.

780 Geyer, W. R. (1993). The importance of suppression of turbulence by stratification on the estuarine turbidity  
781 maximum. *Estuaries*, 16(1):113–125.

782 Gill, A. E. (1982). *Atmosphere—ocean dynamics*. Academic Press.

783 Grant, W. D. and Madsen, O. S. (1982). Movable bed roughness in unsteady oscillatory flow. *Journal of Geophys-*  
784 *ical Research: Oceans*, 87(C1):469–481.

785 Haidvogel, D. B., Arango, H., Budgell, W. P., Cornuelle, B. D., Curchitser, E., Di Lorenzo, E., Fennel, K., Geyer,  
786 W. R., Hermann, A. J., Lanerolle, L., et al. (2008). Ocean forecasting in terrain-following coordinates: For-  
787 mulation and skill assessment of the regional ocean modeling system. *Journal of Computational Physics*,  
788 227(7):3595–3624.

789 James, C. (1994). Evaluation of methods for predicting bend loss in meandering channels. *Journal of Hydraulic*  
790 *Engineering*, 120(2):245–253.

791 James, C., Liu, W., and Myers, W. (2001). Conveyance of meandering channels with marginal vegetation. *Pro-*  
792 *ceedings of the Institution of Civil Engineers-Water and Maritime Engineering*, 148(2):97–106.

793 Kadlec, R. H. (1990). Overland flow in wetlands: vegetation resistance. *Journal of Hydraulic Engineering*,  
794 116(5):691–706.

795 Kalkwijk, J. P. T. and Booij, R. (1986). Adaptation of secondary flow in nearly-horizontal flow. *Journal of*  
796 *Hydraulic Research*, 24(1):19–37.

797 Kranenburg, W. M., Geyer, R., and Ralston, D. K. (2017). Observations of salinity and flow velocity structure in a  
798 narrow and curvy tidal river. In *24th Biennial CERF Conference*. CERF.

799 Kranenburg, W. M., Geyer, W. R., Garcia, A. M. P., and Ralston, D. K. (2019). Reversed lateral circulation in a  
800 sharp estuarine bend with weak stratification. *Journal of Physical Oceanography*.

801 Kunkel, C. M., Hallberg, R. W., and Oppenheimer, M. (2006). Coral reefs reduce tsunami impact in model simu-  
802 lations. *Geophysical research letters*, 33(23).

803 Langbein, W. and Leopold, L. (1966). River meanders-theory of minimum variance. *USGS Prof., Paper 422-H*,  
804 15:1966.

805 Langbein, W. B. and Leopold, L. B. (1970). River meanders and the theory of minimum variance. In *Rivers and*  
806 *river terraces*, pages 238–263. Springer.

807 Leeder, M. R. and Bridges, P. H. (1975). Flow separation in meander bends. *Nature*, 253:1–2.

808 Lentz, S. J., Davis, K. A., Churchill, J. H., and DeCarlo, T. M. (2017). Coral reef drag coefficients–water depth  
809 dependence. *Journal of Physical Oceanography*, 47(5):1061–1075.

810 Leopold, L. B. (1960). *Flow resistance in sinuous or irregular channels*. US Government Printing Office.

811 Leopold, L. B., Collins, J. N., and Collins, L. M. (1993). Hydrology of Some Tidal Channels in Estuarine Marshland  
812 Near San Francisco . *CATENA VERLAG*, 20:469–493.

813 Leopold, L. B. and Wolman, M. G. (1960). River meanders. *Geological Society of America Bulletin*, 71(6):769–  
814 793.

815 Leopold, L. B., Wolman, M. G., and Miller, J. P. (2012). *Fluvial processes in geomorphology*. Courier Corporation.

816 Li, C., Valle-Levinson, A., Atkinson, L. P., Wong, K. C., and Lwiza, K. M. (2004). Estimation of drag coefficient  
817 in James river estuary using tidal velocity data from a vessel-towed adcp. *Journal of Geophysical Research:*  
818 *Oceans*, 109(C3).

819 Marani, M., Lanzoni, S., Zandolin, D., Seminara, G., and Rinaldo, A. (2002). Tidal meanders. *Water Resources*  
820 *Research*, 38(11):7–17–14.

821 Marriott, M. J. (1998). *Hydrodynamics of flow around bends in meandering and compound channels*. PhD thesis,  
822 University of Herfordshire.

823 McCabe, R. M., MacCready, P., and Pawlak, G. (2006). Form drag due to flow separation at a headland. *Journal*  
824 *of physical oceanography*, 36(11):2136–2152.

825 Millar, R. G. (2000). Influence of bank vegetation on alluvial channel patterns. *Water Resources Research*,  
826 36(4):1109–1118.

827 Monismith, S. G., Hirsh, H., Batista, N., Francis, H., Egan, G., and Dunbar, R. B. (2019). Flow and drag in a  
828 seagrass bed. *Journal of Geophysical Research: Oceans*, 124(3):2153–2163.

829 Nanson, R. A. (2010). Flow fields in tightly curving meander bends of low width-depth ratio. *Earth Surface*  
830 *Processes and Landforms: The Journal of the British Geomorphological Research Group*, 35(2):119–135.

831 Nepf, H. (1999). Drag, turbulence, and diffusion in flow through emergent vegetation. *Water resources research*,  
832 35(2):479–489.

- 833 Nezu, I. (1993). Turbulence in open-channel flows. *IAHR-monograph*.
- 834 Nidzieko, N. J., Hench, J. L., and Monismith, S. G. (2009). Lateral Circulation in Well-Mixed and Stratified  
835 Estuarine Flows with Curvature. *Journal of Physical Oceanography*, 39(4):831–851.
- 836 Nikuradse, J. (1933). *Strömungsgesetze in rauhen Rohren*. VDI-Verlag.
- 837 Parsons, D. R. (2003). *Flow separation in meander bends*. PhD thesis, University of Sheffield.
- 838 Pattiaratchi, C., James, A., and Collins, M. (1987). Island wakes and headland eddies: a comparison between  
839 remotely sensed data and laboratory experiments. *Journal of Geophysical Research: Oceans*, 92(C1):783–794.
- 840 Pein, J., Valle-Levinson, A., and Stanev, E. V. (2018). Secondary Circulation Asymmetry in a Meandering, Partially  
841 Stratified Estuary. *Journal of Geophysical Research: Oceans*, 123(3):1670–1683.
- 842 Pingree, R. and Maddock, L. (1980). The effects of bottom friction and earth's rotation on an island's wake. *Journal*  
843 *of the Marine Biological Association of the United Kingdom*, 60(2):499–508.
- 844 Redfield, A. C. (1972). Development of a new england salt marsh. *Ecological monographs*, 42(2):201–237.
- 845 Rogers, J. S., Maticka, S. A., Chirayath, V., Woodson, C. B., Alonso, J. J., and Monismith, S. G. (2018). Connecting  
846 flow over complex terrain to hydrodynamic roughness on a coral reef. *Journal of Physical Oceanography*,  
847 48(7):1567–1587.
- 848 Rozovskii, I. L. (1957). *Flow of water in bends of open channels*. Academy of Sciences of the Ukrainian SSR.
- 849 Schmidt, J. C. (1990). Recirculating flow and sedimentation in the colorado river in grand canyon, arizona. *The*  
850 *Journal of Geology*, 98(5):709–724.
- 851 Schnauder, I. and Sukhodolov, A. (2012). Flow in a tightly curving meander bend: effects of seasonal changes in  
852 aquatic macrophyte cover. *Earth Surface Processes and Landforms*, 37(11):1142–1157.
- 853 Seim, H., Blanton, J., and Elston, S. (2006). Tidal circulation and energy dissipation in a shallow, sinuous estuary.  
854 *Ocean Dynamics*, 56(3-4):360–375.
- 855 Seim, H. E. and Gregg, M. C. (1997). The importance of aspiration and channel curvature in producing strong  
856 vertical mixing over a sill. *Journal of Geophysical Research: Oceans*, 102(C2):3451–3472.
- 857 Seminara, G. (2006). Meanders. *Journal of fluid mechanics*, 554:271–297.



858 Shapiro, A. H. and Sonin, A. A. (2018). *Advanced Fluid Mechanics Problems*. (Self-published manuscript).

859 Shchepetkin, A. F. and McWilliams, J. C. (2005). The regional oceanic modeling system (roms): a split-explicit,  
860 free-surface, topography-following-coordinate oceanic model. *Ocean modelling*, 9(4):347–404.

861 Signell, R. P. and Geyer, W. R. (1991). Transient eddy formation around headlands. *Journal of Geophysical*  
862 *Research: Oceans*, 96(C2):2561–2575.

863 Thackston, E. L. and Schnelle, K. B. (1970). Predicting effects of dead zones on stream mixing. *Journal of the*  
864 *Sanitary Engineering Division*, 96(2):319–331.

865 Thomson, J. (1877). V. on the origin of windings of rivers in alluvial plains, with remarks on the flow of water  
866 round bends in pipes. *Proceedings of the Royal Society of London*, 25(171-178):5–8.

867 Umlauf, L. and Burchard, H. (2003). A generic length-scale equation for geophysical turbulence models. *Journal*  
868 *of Marine Research*, 61(2):235–265.

869 Warner, J. C., Armstrong, B., He, R., and Zambon, J. B. (2010). Development of a coupled ocean–atmosphere–  
870 wave–sediment transport (coawst) modeling system. *Ocean modelling*, 35(3):230–244.

871 Warner, J. C., Sherwood, C. R., Arango, H. G., and Signell, R. P. (2005). Performance of four turbulence closure  
872 models implemented using a generic length scale method. *Ocean Modelling*, 8(1-2):81–113.

873 Warner, S. J. and MacCready, P. (2014). The dynamics of pressure and form drag on a sloping headland: Internal  
874 waves versus eddies. *Journal of Geophysical Research: Oceans*, 119(3):1554–1571.

875 Wolanski, E., Imberger, J., and Heron, M. L. (1984). Island wakes in shallow coastal waters. *Journal of Geophysical*  
876 *Research: Oceans*, 89(C6):10553–10569.

877 Zhong, L. and Li, M. (2006). Tidal energy fluxes and dissipation in the chesapeake bay. *Continental Shelf Research*,  
878 26(6):752–770.